

# H II Region Metallicity Distribution in the Milky Way Disk

Dana S. Balser<sup>1</sup>, Robert T. Rood<sup>2</sup>, T. M. Bania<sup>3</sup>, & L. D. Anderson<sup>3,4</sup>

## ABSTRACT

The distribution of metals in the Galaxy provides important information about galaxy formation and evolution. H II regions are the most luminous objects in the Milky Way at mid-infrared to radio wavelengths and can be seen across the entire Galactic disk. We used the NRAO Green Bank Telescope (GBT) to measure radio recombination line and continuum emission in 81 Galactic H II regions. We calculated LTE electron temperatures using these data. In thermal equilibrium metal abundances are expected to set the nebular electron temperature with high abundances producing low temperatures. Our H II region distribution covers a large range of Galactocentric radius (5 to 22 kpc) and samples the Galactic azimuth range  $330^\circ$  to  $60^\circ$ . Using our highest quality data (72 objects) we derived an O/H Galactocentric radial gradient of  $-0.0383 \pm 0.0074$  dex  $\text{kpc}^{-1}$ . Combining these data with a similar survey made with the NRAO 140 Foot telescope we get a radial gradient of  $-0.0446 \pm 0.0049$  dex  $\text{kpc}^{-1}$  for this larger sample of 133 nebulae. The data are well fit by a linear model and no discontinuities are detected. Dividing our sample into three Galactic azimuth regions produced significantly different radial gradients that range from  $-0.03$  to  $-0.07$  dex  $\text{kpc}^{-1}$ . These inhomogeneities suggest that metals are not well mixed at a given radius. We stress the importance of homogeneous samples to reduce the confusion of comparing data sets with different systematics. Galactic chemical evolution models typically derive chemical evolution along only the radial dimension with time. Future models should consider azimuthal evolution as well.

*Subject headings:* Galaxy: abundances — ISM: H II regions — radio lines: ISM

---

<sup>1</sup>National Radio Astronomy Observatory, 520 Edgemont Rd., Charlottesville, VA 22903, USA.

<sup>2</sup>Astronomy Department, University of Virginia, P.O. Box 400325, Charlottesville VA 22904-4325, USA.

<sup>3</sup>Institute for Astrophysical Research, Department of Astronomy, Boston University, 725 Commonwealth Avenue, Boston MA 02215, USA.

<sup>4</sup>Current address: Laboratoire d'Astrophysique de Marseille (UMR 6110 CNRS & Université de Provence), 38 rue F. Joliot-Curie, 13388 Marseille Cedex 13, France.

## 1. Introduction

Galactic chemical evolution (GCE) models are important for understanding how galaxies form and evolve. A key observational constraint for these models is the spatial and temporal distribution of abundances in the Galaxy (Pagel 1997; Chiappini et al. 1997; Tosi 2000; Prantzos 2003; Carigi et al. 2005; Colavitti et al. 2008; Fu et al. 2009; Schönrich & Binney 2009, and references within). The isotopes of hydrogen, helium, and lithium were produced in the Big Bang (e.g., Steigman 2007). Further processing, primarily in low-mass ( $< 2 M_{\odot}$ ) stars, altered these primordial abundances through many generations of star formation and evolution in the Galaxy, therefore light element abundance measurements yield important constraints for models of Big Bang nucleosynthesis and low-mass stellar evolution (Boesgaard & Steigman 1985; Wilson & Rood 1994; Steigman 2007, and references within).

In contrast, heavier elements or metals are produced in higher mass stars. The two most common abundance tracers of metallicity are iron and oxygen since they have bright spectral lines and are a measure of heavy element production from hydrogen (Henry & Worthey 1999). Iron absorption lines are typically observed in stars, while oxygen emission lines are observed in the interstellar medium (ISM). All optical diagnostics within the disk are restricted to the local Solar neighborhood because of extinction from dust. While far infrared tracers penetrate the dust, they are significantly weaker than their optical counterparts.

Early studies of radio recombination line (RRL) and continuum emission toward H II regions revealed positive Galactic radial gradients of the derived electron temperatures (Churchwell & Walmsley 1975; Churchwell et al. 1978; Wink et al. 1983; Shaver et al. 1983). The electron temperature radial gradient was interpreted as a metallicity gradient since the balance of heating and cooling within H II regions is sensitive to the abundance of metal coolants, such as carbon and oxygen. Shaver et al. (1983) calibrated the electron temperature-metallicity relation by comparing oxygen abundances from collisionally excited lines with derived electron temperatures from RRLs. Over the last decade, significant improvements in telescope instrumentation have increased the sensitivity of RRL observations (e.g., Balser 2006; von Procházka et al. 2010) and increased the Galactic H II region sample size (Bania et al. 2010; Anderson et al. 2011). Here we discuss new RRL and continuum measurements made with the National Radio Astronomy Observatory (NRAO)<sup>1</sup> Green Bank Telescope (GBT).

---

<sup>1</sup>The National Radio Astronomy Observatory is a facility of the National Science Foundation operated under cooperative agreement by Associated Universities, Inc.

## 2. H II Region Target Sample

We selected H II regions from the following catalogs: Felli & Churchwell (1972); Felli et al. (1978); Shaver et al. (1983); Digel et al. (1994); Lockman (1989); Lockman et al. (1996); Rudolph et al. (1996, 1997); Brand & Wouterloot (2007); Anderson et al. (2011). The H II region sample was chosen, in part, to compliment the NRAO 140 Foot telescope survey made by Quireza et al. (2006a); hereafter called the “140 Foot Sample”. We specifically selected H II regions at large Galactocentric radius to study the radial metallicity gradient discontinuity at 10 kpc suggested by several studies (e.g., Twarog et al. 1997). Quireza et al. (2006b) identified possible structure in the azimuthal distribution of nebular electron temperature so we chose sources that produced a more uniform spatial distribution between Galactic azimuth  $330^\circ$  and  $60^\circ$ . Only objects that were well isolated, so that a continuum zero-level could be measured, and bright enough to accurately measure the RRL parameters were chosen. We re-observed 28 objects from Quireza et al. (2006b) for cross-calibration.

Table 1 summarizes the properties of our GBT H II region sample; hereafter called the “GBT Sample”. Listed are the source name, the Galactic and Equatorial coordinates, the Galactocentric azimuth,  $Az$ , and radius,  $R_{\text{gal}}$ , the distance from the Sun,  $d_{\text{Sun}}$ , the helium abundance ratio by number,  $y$ , and the LTE electron temperature,  $T_e$ . Details about the derivation of helium abundances and electron temperatures are given in §4.1. Figure 1 shows both H II regions samples, hereafter called the “Green Bank Sample”, projected onto the Galactic plane. Plotted are the GBT Sample (green points) and the 140 Foot Sample (blue crosses) as a function of Galactocentric position ( $Az$ ,  $R_{\text{gal}}$ ). The GBT Sample includes 44 H II regions at  $R_{\text{gal}} > 10$  kpc compared with only 26 sources for the 140 Foot Sample.

We can determine kinematic distances for all but two of the H II regions in our sample. Kinematic distances are derived using the measured source velocity and a rotation curve model for the Galaxy. For all kinematic distances we use our measured hydrogen RRL velocities (see Table 2) and the Brand (1986) rotation curve model. In the inner Galaxy, rotation curve models have two possible distances for each measured velocity, a “near” and a “far” distance. This problem is known as the “kinematic distance ambiguity,” or KDA, and to resolve it one must use auxiliary data. For H II regions, H I along the line of sight, which emits at 21 cm, will absorb against the broadband H II region continuum. H I is nearly ubiquitous in our Galaxy and emits at all allowed velocities. The maximum velocity of detected absorption in an H I spectrum in the direction of an H II region can distinguish between the near and the far distance (see Kuchar & Bania 1994; Fish et al. 2003; Kolpak et al. 2003; Anderson & Bania 2009). Using the H I absorption spectrum to resolve the KDA is known as the H I Emission/Absorption (H I E/A) method.

Our sample contains 22 inner Galaxy H II regions affected by the KDA. For the seven

sources in common with Anderson & Bania (2009), we use their KDA resolution. These sources are: G32.797+0.19 (far), G46.495–0.25 (near), G52.75+0.3 (far), K47 (far), NRAO584 (near), W51 (near), and W43 (far). There are four inner Galaxy sources in our sample that are not in Anderson & Bania (2009). For these we make an H I E/A measurement using the 21 cm H I VLA Galactic Plane Survey (Stil et al. 2006) and apply the same methodology as Anderson & Bania (2009). For S87, S88, and S93, we conclude that the near distance is more consistent with the H I absorption spectrum, whereas for S90 the H I absorption spectrum supports the far distance. For two additional inner Galaxy sources not included in Anderson & Bania (2009), S76 and W48, there is no public H I data at sufficient angular resolution to perform the H I E/A method. For these two sources, we assume the KDA resolution given in Quireza et al. (2006b) and place both sources at the near kinematic distance. One additional source, G39.728–0.396, is part of the GBT H II Region Discovery Survey (Bania et al. 2010; Anderson et al. 2011), and we use the far kinematic distance from L. Anderson et al. (2011, in preparation). There are seven H II regions whose RRL velocity is within  $10 \text{ km s}^{-1}$  of the tangent point velocity, which is the maximum velocity along the line of sight: G78.03+0.6, G79.42+2.4, G80.88+0.4, G81.25+1.1, S106, S108, and S112. The KDA resolutions for such sources are unreliable and we therefore locate them at the tangent point distance. The remaining 62 sources are in the outer Galaxy and are thus not affected by the KDA.

There are two sources with kinematic distances that are clearly incorrect. For Orion A (“OriA” in Tables 1-3), the measured RRL velocity of  $-2.25 \text{ km s}^{-1}$  is not defined for its Galactic location in the Brand (1986) rotation curve. We instead use a distance of 0.4 kpc (Menten et al. 2007), which was derived using VLBI maser parallax measurements. S235 is located near the Galactic anti-center and the measured velocity of  $-25.61 \text{ km s}^{-1}$  produces an unreliable kinematic distance using the Brand (1986) rotation curve. We instead use a distance of 1.6 kpc for this source (Fich et al. 1989; Blitz et al. 1982), as in Bania et al. (1997).

We choose to use kinematic distances here since we are able to derive kinematic distances to almost all of our sources, thus providing a homogeneous sample for our electron temperature analysis. The radial gradients, moreover, do not suffer from the KDA since they only depend on  $R_{\text{gal}}$ . Reliably detecting azimuthal structure, however, does require  $d_{\text{Sun}}$  and that we resolve the KDA. In future work we shall make further analyzes of the Galactic distribution of nebular  $T_e$  by including spectroscopic and trigonometric parallaxes, especially those made using VLBI measurements of H II region masers. It is the case, however, that the  $\sim 20\%$  errors typically found for kinematic distances are much smaller than the separation between a source’s near and far kinematic distance. We should thus have sufficient accuracy in the distances that we use here to resolve azimuthal structure in the  $T_e$  distribution on

scales of approximately a few kpc.

### 3. Observations

Here we discuss RRL and continuum observations at X-band (8 to 10 GHz) toward 81 Galactic H II regions with the GBT. The spectral line data consist of total power, position switched spectra in which a reference position (Off) was observed offset  $\sim 6$  minutes in right ascension from the source and then the target position (On) was observed. The reference and target positions were observed for 6 minutes each for a total of 12 minutes. The GBT auto-correlation spectrometer (ACS) was configured with 8 spectral windows, hereafter sub-bands, and two orthogonal, circular polarizations for a total of 16 independent spectra. Each sub-band had a bandwidth of 50 MHz and 4096 channels, yielding a frequency resolution of 12.2 kHz. These spectra included 7 Hn $\alpha$  RRLs (H87 $\alpha$  to H93 $\alpha$ ) that span the range of the X-band receiver with half-power beam-widths (HPBW) from 73 to 90 arcsec.<sup>2</sup> The center rest frequencies were: 8045.60495992323, 8300.0, 8584.82315062037, 8665.3, 8877.0, 9183.0, 9505.0, and 9812.0 MHz.

We measured the H II region continuum emission with the GBT Digital Continuum Receiver (DCR) by scanning in R.A. and Decl. through the center of the source at a frequency of 8665 MHz and a bandwidth of 320 MHz. The catalog target coordinates were updated based on GBT pointing observations in R.A. and Decl.—that is, we peaked up on each H II region. Each continuum observation consisted of 4 scans, whereby the telescope was driven at a rate of 80 arcmin per minute in both the forward and backward directions in R.A. and then in Decl. Data were simultaneously taken at two orthogonal, circular polarizations and were sampled every 0.1 s over an angular path 40 arcmin in length.

Details of the data reduction and calibration are discussed in Appendix A. To increase the signal-to-noise ratio the 7 Hn $\alpha$  RRLs were averaged. In the final averaged RRL spectra we excluded the H90 $\alpha$  RRL because nearby, higher order RRLs made it difficult to measure a good spectral baseline. The averaging process required three steps: (1) the velocity scale of the H88 $\alpha$  to H93 $\alpha$  RRLs were re-gridded to the velocity scale of the H87 $\alpha$  RRL; (2) the RRL spectra were shifted to match the Doppler tracked H89 $\alpha$  RRL; and (3) the intensity scale was adjusted to correct for the different HPBWs by assuming Gaussian source brightness distributions and HPBWs. The primary goal here is to calculate the nebular electron

---

<sup>2</sup>Our configuration is identical to Balser (2006) except we replaced the sub-band centered at the H86 $\alpha$  line, which is confused by higher order RRL transitions, with a sub-band centered at 8665.3 MHz. This sub-band includes the H114 $\beta$  and H130 $\gamma$  RRLs that are used to monitor system performance.

temperature which is a function of the line-to-continuum ratio. Since the electron temperature is derived from this ratio of two intensities, many observing errors cancel and therefore a relative flux scale calibration is sufficient. We used all target sources with a continuum antenna temperature  $> 5$  K to derive an average relative calibration accurate to within 5%.

The data were analyzed using TMBIDL, an IDL single-dish software package.<sup>3</sup> The line and continuum parameters were determined after the data reduction and calibration. For each spectral average we typically modeled the baseline with a third-order polynomial function that was subtracted from the data. The hydrogen, helium, and carbon RRL profiles were fit with a Gaussian function using a Levenberg-Marquardt least-squares method (Markwardt 2009) to derive the peak intensity, the full-width half-maximum (FWHM) line width, and the LSR velocity. The continuum data were analyzed in a similar way. A polynomial function was used to model the background signal and to measure the zero level. The background emission consists of the non-thermal Galactic background, the atmosphere, and receiver noise. The R.A. and Decl. scans were independently modeled with Gaussian functions to derive the peak continuum intensity and the angular FWHM source size in each direction.

#### 4. Results

Table 2 lists the Gaussian parameters of the H, He, and C RRLs together with their associated errors. These include the peak intensity,  $T_L$ , the FWHM line width,  $\Delta V$ , and the LSR<sup>4</sup> velocity,  $V_{\text{LSR}}$ . Also shown are the total integration time,  $t_{\text{intg}}$ , and the root-mean-square noise of the line free region,  $rms$ . The integration time listed in Table 2 is derived from the spectral average of both polarizations of the H87 $\alpha$ , H88 $\alpha$ , H89 $\alpha$ , H91 $\alpha$ , H92 $\alpha$ , and H93 $\alpha$  transitions. Helium and carbon RRLs were detected in 66% and 33% of the H II region targets, respectively. Sample RRL spectra that range from our best to worse quality data are shown in Figure 2. The antenna temperature is plotted as a function of LSR velocity. The velocity scale is referenced with respect to the H89 $\alpha$  RRL.

Table 3 lists the radio continuum Gaussian parameters for the peak intensity,  $T_C$ , and FWHM angular width,  $\Theta$ , for the R.A. scans and the Decl. scans, together with the average source properties. We use the arithmetic mean for the average peak intensity and the geo-

---

<sup>3</sup>See <http://www.bu.edu/iar/files/script-files/research/dapsdr/index.html>.

<sup>4</sup> The RRL velocities here are in the kinematic local standard of rest (LSR) frame using the radio definition of the Doppler shift. The kinematic LSR is defined by a solar motion of  $20.0 \text{ km s}^{-1}$  toward  $(\alpha, \delta) = (18^{\text{h}}, +30^{\circ})$  [1900.0] (Gordon 1976).

metric mean for the average FWHM width. Sample continuum scans are shown in Figure 3. The antenna temperature is plotted as a function of the offset sky position relative to the target coordinates listed in Table 1. Both the R.A. and Decl. scans are displayed for the Figure 2 H II regions.

Following Quireza et al. (2006a) we assign a letter grade, called the quality factor or QF, to the line and continuum data for each source. The QF is a measure of data quality taking into account the signal-to-noise ratio,  $snr$ , the baselines, confusion, and the Gaussian fit. The errors in the Gaussian fit and the  $rms$  baseline noise yield a quantitative measure of the data quality, but these metrics do not assess systematic uncertainties. For example, a poor fit of the baseline can result in significant errors in the peak intensity that are not reflected by the formal errors. For the continuum data the QF was determined by visual inspection of the data, including the baseline and Gaussian fits as is described in Quireza et al. (2006a). The QF scale ranges from A (excellent) to D (poor).

Visual inspection of the spectral line data revealed little variation in the quality of the spectral baselines—the spectral baselines were excellent. Unlike the 140 Foot telescope spectra, the unblocked aperture of the GBT yields significantly improved spectral baselines. Moreover, we selected H II region targets with a single component H RRL so there was no line confusion. For these reasons we derived the QF for the H RRLs quantitatively using the  $snr$  and the percent error in the Gaussian fit of the line area,  $\epsilon_a = 100 (\sigma T_L \sigma \Delta V) / (T_L \Delta V)$ . We assigned the spectral line QF in the following way: A ( $snr \geq 50$ ,  $\epsilon_a \leq 1.0$ ); B ( $50 > snr \geq 20$ ,  $1.0 < \epsilon_a \leq 2.0$ ); C ( $20 > snr \geq 7.5$ ,  $2.0 < \epsilon_a \leq 5.0$ ); or D otherwise. The QF’s are listed in the last column of Tables 2 and 3. The QF distribution for the RRLs is: 22 A, 25 B, 31 C, 3 D. For the continuum it is: 19 A, 38 B, 18 C, and 6 D. Thus 96% of the RRLs have QFs of C or better whereas 93% of the continuum scans have QFs of C or better.

#### 4.1. Electron Temperature

Following Quireza et al. (2006b) we derived the LTE electron temperature using the equation:

$$\left(\frac{T_e}{K}\right) = \left[7103.3 \left(\frac{\nu_L}{\text{GHz}}\right)^{1.1} \left(\frac{T_C}{T_L(\text{H}^+)}\right) \left(\frac{\Delta V(\text{H}^+)}{\text{km s}^{-1}}\right)^{-1} (1+y)^{-1}\right]^{0.87} \quad (1)$$

where

$$y \equiv \frac{n(^4\text{He}^+)}{n(\text{H}^+)} = \frac{T_L(^4\text{He}^+) \Delta V(^4\text{He}^+)}{T_L(\text{H}^+) \Delta V(\text{H}^+)}, \quad (2)$$

and  $\nu_L$  is the H RRL rest frequency,  $T_C$  is the continuum peak intensity,  $T_L$  is the H or He RRL intensity, and  $\Delta V$  is the H or He RRL FWHM line width. We used  $\nu_L = 9$  GHz, the average H RRL frequency. The values of  $T_e$  and  $y$  are listed in Table 1 for each H II region. The uncertainties were calculated by propagating the Gaussian fitting errors through Equation 1 for the line and continuum observations. As discussed by Quireza et al. (2006b), the LTE electron temperature should be a very good approximation to the real average nebular electron temperature. Non-LTE effects, such as stimulated emission and pressure broadening from electron impacts should be small.

Helium RRL emission was not detected in 27 of the 81 H II regions. In these cases we estimated an upper limit for  $y$  by assuming  $T_L(^4\text{He}^+) = 3 * rms$  and  $\Delta V(^4\text{He}^+) = 0.75 \Delta V(\text{H}^+)$ . This is consistent with gas at  $T_e = 8000$  K and a hydrogen FWHM line width of  $25 \text{ km s}^{-1}$ . In all cases the upper limit is larger than the canonical value of the He/H abundance ratio (0.08; see Quireza et al. 2006b), indicating that we lack the sensitivity to detect helium emission in these objects and not that these H II regions have low excitation. For sources with no detected helium emission we therefore assume  $y = 0.08$  and list them with zero errors in Table 1. Nonetheless, the electron temperature is not very sensitive to  $y$ . Using Equation 1 and parameter values typical of our H II region sample, a 10% change in  $y$  results in only a 0.6% change in  $T_e$ .

Figure 4 compares the electron temperatures derived for nebulae that are in both the GBT and 140 Foot samples. We only plot sources that have a QF of C or better for both line and continuum data. For these 16 objects the mean value of the electron temperature is  $8813 \pm 1114$  K and  $8844 \pm 1084$  K for the GBT Sample and the 140 Foot Sample, respectively. While there is no systematic variation in electron temperature there are differences in  $T_e$  that are significantly larger than the formal error. The error bars shown in Figure 4 correspond to the measurement errors and do not include calibration errors. We estimate that errors in  $T_e$  due to calibration are less than 5% for the GBT (see Appendix B) and less than 10% for the 140 Foot telescope (see §5.1 in Quireza et al. (2006b)). Since the telescope HPBW's vary by a factor of 2.4, moreover, we are sampling different volumes of nebular gas and so cannot rule out true fluctuations in  $T_e$  within each nebula that can vary by as much as 10% (e.g., Roelfsema et al. 1992).

## 4.2. Electron Temperature Radial Gradient

The electron temperature radial gradient is plotted in Figure 5 for the GBT Sample (top panel) and the Green Bank Sample (bottom panel). Only sources with QFs C or better for both the line and continuum data are included. For clarity we do not display the electron



temperature errors which are typically less than 5%. As was also found by Quireza et al. (2006b), these errors are significantly smaller than the dispersion of the data points. For example, using the GBT Sample the *rms* of the measured electron temperatures relative to the fitted value is 854 K, or 9% of the mean electron temperature. The dispersion for the Green Bank Sample is larger, especially for  $R_{\text{gal}} < 10$  kpc. This can be explained by the presence of azimuthal structure because the azimuth range sampled by our H II regions with  $R_{\text{gal}} < 10$  kpc is larger (see Figure 1 and below). The solid lines are least-squares linear fits to the data. The program SLOPES<sup>5</sup> was used to perform an ordinary least-squares regression using asymptotic error formulae (Isobe et al. 1990; Feigelson & Babu 1992). These uncertainties are valid for  $N > 50$  but underestimate the true error for a smaller sample. We used the jackknife resampling procedure in SLOPES to derive more accurate uncertainties for smaller samples, although the slopes are unchanged. The electron temperature radial gradient fits are shown in Tables 4 and 5 for the GBT Sample and the Green Bank Sample, respectively. Listed are the azimuth range of the nebulae included in each fit, the fitted coefficients  $a$  and  $b$  (where  $T_e = a + b R_{\text{gal}}$ ), the correlation coefficient,  $r$ , the number of H II regions in each fit sample,  $N$ , and the Galactocentric radius range of the sample nebulae. The uncertainties for the correlation coefficient were derived using the jackknife method discussed by Efron et al. (1979). The fit for the GBT Sample is consistent with the gradient measured for Sample B by Quireza et al. (2006b) using the 140 Foot telescope. Sample B includes all H II regions with QF values of C and better. *Quireza et al. (2006b) made an error in their determination of the continuum temperature of S209N.* Here we derive  $T_e = 10310 \pm 360$  K for S209N. A linear fit to their Sample B now gives:  $a = 5856 \pm 340$  K and  $b = 254 \pm 41$  K kpc<sup>-1</sup>. This corresponds to a 20% change in  $T_e$  for S209N and a 10% change in the slope. Since  $R_{\text{gal}} = 16.7$  kpc for S209N it has significant leverage in the fit for  $b$ .

We explored azimuthal structure in the electron temperature gradient by dividing the data into three azimuth ranges:  $330^\circ < Az < 360^\circ$ ;  $0^\circ < Az < 30^\circ$ ; and  $30^\circ < Az < 60^\circ$ . Figure 6 plots the electron temperature radial gradient for each azimuth range, and Tables 4 and 5 list the linear least-squares fit parameters. The data within each azimuth range are well modeled by a linear fit with correlation coefficients between 0.62 – 0.88. The gradient varies significantly within each azimuth range with a smaller slope between azimuth 0 – 30°.

To visualize structure in the electron temperature distribution in the Galactic plane we employed Shepard’s method to interpolate the electron temperature values over the discrete H II region locations (Shepard 1968; Gordon & Wixom 1978). Shepard (1968) developed an algorithm to interpolate over arbitrarily spaced, discrete data. Gordon & Wixom (1978)

---

<sup>5</sup>See <http://www.astro.psu.edu/users/edf/research/stat.html>.

introduced a free parameter,  $\alpha$ , that when increased flattens the resulting image near the discrete data locations. Figure 7 plots the results of this interpolation when applied to the Green Bank Sample for  $\alpha = 5$ . The black points denote the location of the H II regions used in the interpolation (cf. Figure 1). The interpolated image is represented by the contour map. The contour levels range between 6400 and 11200 K at intervals of 400 K. The darker shades are lower temperatures. We only included data spanning an azimuth range from  $330^\circ$  to  $60^\circ$ . The radial  $T_e$  gradients are visible at all Galactocentric azimuths with higher electron temperatures at larger  $R_{\text{gal}}$ . At a constant Galactocentric radius the electron temperature is not constant, revealing azimuthal structure and that the gas is not well mixed in the Galaxy. Positions in the Galaxy that are located far from any of our H II regions have an interpolated electron temperature equal to the average  $T_e$  value in our sample.

### 4.3. O/H Abundance Ratio

The metallicity is the dominant factor that controls the H II region equilibrium electron temperature. There are at least four physical properties that effect H II region electron temperatures: the effective temperature of the ionizing star, the electron density of the surrounding medium, dust-particle interactions, and the metallicity. The stellar effective temperature,  $T_{\text{eff}}$ , sets the hardness of the radiation field that excites and heats the gas. Rubin (1985) predicts an increase in  $T_e$  of 1300 K for a change in  $T_{\text{eff}}$  from 33,000 to 45,000 K (B0 to O5 spectral type). The electron density,  $n_e$ , alters the rate of collisional de-excitation. High values of  $n_e$  will inhibit cooling and thus increase  $T_e$ . Rubin (1985) estimates an increase in  $T_e$  of 2900 K for a change in  $n_e$  from 100 to  $10^5 \text{ cm}^{-3}$ . Dust effects the electron temperature in complex ways: photo-electric heating occurs as electrons are ejected from dust grains and collide with atoms, whereas cooling of the gas can result when there are collisions of fast particles with dust grains (Mathis 1986; Baldwin et al. 1991; Shields & Kennicutt 1995). Oliveira & Maciel (1986) estimate that the net effect of dust is on the order of 500 K. Heavy elements within the ionized gas will increase the cooling primarily through collisionally excited lines and lower  $T_e$  (Garay & Rodríguez 1983). Rubin (1985) predicts changes in  $T_e$  of 7,000 K for a factor of 10 change in metal abundance.

Given the typical range of values for these physical properties in Galactic H II regions, the metallicity should thus be the dominant factor in producing variations in the electron temperature. We explored, for example, the effects of density and excitation on the derived electron temperatures for the GBT Sample. Assuming that each H II region is a spherical, homogeneous, optically thin nebula we derived the electron density using Equation G7 by Balser (1995). (See Quireza et al. (2006b) for a similar analysis.) To assess the effect of

excitation we calculated the number of H-ionizing photons emitted per second,  $N_L$ , as a proxy for  $T_{\text{eff}}$  using Equation G9 by Balser (1995). This provides an upper limit to  $T_{\text{eff}}$  since more than one early-type star may be ionizing the nebula. We found no significant correlation of the electron temperature with the electron density ( $r = 0.10$ ) or  $N_L$  ( $r = 0.03$ ), where  $r$  is the correlation coefficient. This suggests that metallicity is the most important factor in determining the electron temperature for our sample of H II regions.

Given the homogeneity of our sample, the derived electron temperatures should provide an excellent proxy for metallicity. Following Shaver et al. (1983), we divided our H II regions into two groups having either high or low values of both  $N_L$  or  $n_e$ . The threshold values were  $\text{Log}(N_L) = 49.5 \text{ s}^{-1}$  and  $n_e = 150 \text{ cm}^{-3}$ . Similar to Wink et al. (1983) and Quireza et al. (2006b) we find no systematic trend in the electron temperature for these two samples. Shaver et al. (1983) found that the high ( $n_e$ ,  $N_L$ ) sample produced higher values of  $T_e$  for a given Galactocentric radius. But this trend is weak since the correlation is strongest at small  $R_{\text{gal}}$ , where there are systematically low  $T_e$  values (Quireza et al. 2006b). The physical effect of  $n_e$  on the electron temperature has clearly been observed, however, by comparing electron temperatures derived from single-dish telescopes with those from interferometers. Afflerbach et al. (1996) observed RRLs with the VLA toward ultracompact H II regions and found electron temperatures about 1000 K hotter than the Shaver et al. (1983) single-dish values. Interferometers are sensitive to compact, high density gas, whereas single-dish telescopes probe the more extended, low density gas.

We calculated O/H abundance ratios from our H II region electron temperatures using the relationship derived by Shaver et al. (1983). This is based on electron temperatures from RRL and continuum emission and collisionally excited lines (CELs) of oxygen. They estimate an *rms* uncertainty of 0.1 dex in  $\text{Log}(\text{O}/\text{H})$ . Pilyugin et al. (2003) claim that the oxygen abundances calculated by Shaver et al. (1983) are systematically overestimated by 0.2 – 0.3 dex. They determined O/H abundance ratios using the P-method, where an excitation parameter is employed to derive the physical conditions in the H II regions. Regardless, any systematic O/H abundance calibration error should not effect gradient measurements. The Shaver et al. (1983) relationship between  $\text{Log}(\text{O}/\text{H})$  and  $T_e$  is:

$$12 + \text{Log}(\text{O}/\text{H}) = (9.82 \pm 0.02) - (1.49 \pm 0.11) T_e/10^4. \quad (3)$$

Here we only use CELs to convert electron temperatures to O/H abundance ratios. Some authors have advocated the use of optical recombination lines (ORLs) since, unlike CELs, deriving the O/H abundance ratio using ORLs is not a strong function of the electron temperature or density structure (e.g., Esteban et al. 2005). O/H abundance ratios derived from ORLs are typically larger than those determined from CELs. This trend is observed with several abundance tracers in both H II regions and planetary nebulae and is called the

“abundance discrepancy problem” (García-Rojas et al. 2007a). García-Rojas et al. (2007b) suggest that the problem stems from the presence of temperature fluctuations, whereas Liu et al. (2000) argue that it comes from hydrogen deficient clumps in the nebula. Recently, Nahar et al. (2010) have suggested that the abundance discrepancy problem is caused by an underestimate of the low-temperature ( $10^2$ – $10^4$  K) dielectronic recombination rates. Based on theoretical calculations they argue that resonant features in the low-energy photoionization cross section of O II must be included. They are in the process of calculating recombination rate coefficients into all recombined levels of O II up to  $n = 10$ .

Regardless of how accurately we can measure the O/H abundance, this ratio corresponds to the gas phase abundance and does not account for depletion of oxygen onto dust grains. Peimbert & Peimbert (2010) estimate an oxygen depletion that varies from about 0.08 dex for the most metal poor H II regions to 0.12 dex for the most metal rich H II regions with an uncertainty of about 0.03 dex. Given the small changes in the O/H abundance ratio and the large uncertainty we assume oxygen depletion onto dust grains is negligible.

Our O/H radial gradient fits are summarized in Table 6 and Figure 8 which plots the O/H abundance ratio derived from Equation 3 as a function of  $R_{\text{gal}}$  for the GBT Sample (top) and the Green Bank Sample (bottom). The data are divided into the same azimuth ranges as shown in Figure 6. The O/H gradient varies from about  $-0.03$  to  $-0.07$  dex  $\text{kpc}^{-1}$  depending on the Galactic azimuth.

## 5. Discussion

Studies of chemical evolution are important because they connect to many other fields of astronomy, such as cosmology, stellar nucleosynthesis, and the origin and evolution of galaxies (King 1971; van den Bergh 1975; Peimbert 1975; Trimble 1975; Audouze & Tinsley 1976; Pagel & Edmunds 1981; Henry & Worthey 1999). Measuring the spatial and temporal distribution of abundances is a key constraint to understanding chemical evolution in galaxies. Radial gradients were first detected in nearby galaxies from optical observations of CELs of oxygen, nitrogen, and sulfur in H II regions (Searle 1971; Rubin et al. 1972; Smith 1975). Similar measurements in the Milky Way disk are significantly more sensitive but they are hampered by extinction from dust and the difficulty of determining relative positions within the disk. RRLs provide a unique probe of metallicity since H II regions can be detected at radio frequencies throughout the Galactic disk (Bania et al. 2010; Anderson et al. 2011), and significant progress has been made in deriving accurate distances (Anderson & Bania 2009; Reid et al. 2009). Here we summarize previous abundance measurements in the Galactic disk, discuss our GBT RRL results, and explore how these data can constrain chemical

evolution models.

### 5.1. Previous Studies

The primary tracers of metals in the Galactic disk are open clusters, Cepheids, OB stars, planetary nebulae, and H II regions. Open clusters cover a wide range of metallicity and age (30 Myr to 11 Gyr); hence they directly probe metallicity with time (Friel 1995). Early studies of abundances in open clusters were based on photometry with radial metallicity gradients of  $-0.05 \pm 0.01 \text{ dex kpc}^{-1}$  (Janes 1979). More recent work has focused on spectroscopic measurements that provide an abundance and a velocity that can be used to determine cluster membership. Friel et al. (2002) measured a radial gradient of  $0.059 \pm 0.010 \text{ dex kpc}^{-1}$  from a sample of 39 open clusters. They found evidence for a flattening of the radial gradient with time:  $-0.072 \pm 0.016 \text{ dex kpc}^{-1}$  and  $-0.046 \pm 0.012 \text{ dex kpc}^{-1}$  for open clusters older and younger than 3 Gyr, respectively (also see Chen et al. 2003). Twarog et al. (1997) analyzed 76 open clusters using photometry and spectroscopy and suggested that there is a discontinuity in the radial abundance distribution near 10 kpc. They associated this break in the radial abundance with the edge of the initial Galactic disk as defined by the disk globular clusters or the thick disk. More recent observations of open clusters in the outer Galaxy support their findings with a break in the radial gradient near 10 kpc and a flattening in the outer Galaxy (Yong et al. 2005; Sestito et al. 2008; Andreuzzi et al. 2010). The shallow slope in the outer Galaxy does not appear to be caused by accretion of metal poor extragalactic material (e.g, dwarf galaxies). Measurements of the location, kinematics, and chemistry of outer Galaxy open clusters are consistent with these objects being part of the Galactic disk (Carraro et al. 2007).

Cepheids are bright, evolved stars that are detected at large distances and are relatively young ( $< 200 \text{ Myr}$ ). They are easy to identify and the photometric distances are reasonably accurate. Many studies using Cepheids support non-uniform radial gradients (Caputo et al. 2001; Andrievsky et al. 2002; Luck et al. 2003; Andrievsky et al. 2004; Pedicelli et al. 2009). Furthermore, there is evidence of chemical inhomogeneities across the Galactic quadrants (Luck et al. 2006; Lemasle et al. 2008; Pedicelli et al. 2009). Using a sample of 24 Cepheids spanning  $R_{\text{gal}}$ 's between 12 and 17.2 kpc, Yong et al. (2006) measured a radial distribution that flattens at 14 kpc, in contrast to the older population open clusters that flatten at 10 kpc. Since the Cepheid population is younger than the open cluster population this suggests that the Galactic disk has grown in radius by a few kpc over the past several billion years via accretion. Young et al. find a bimodal  $[\text{Fe}/\text{H}]$  distribution in their outer Galaxy sample with one population, “Galactic Cepheids”, that agrees with the extrapolation of the gradient

measured at smaller  $R_{\text{gal}}$ , and another population, “Merger Cepheids”, with significantly lower values of  $[\text{Fe}/\text{H}]$ .

OB-type stars are young ( $< 10$  Myr) and their abundances trace the metallicity near their current location. This assumes that mixing in the outer layers of OB-type stars is negligible (Sofia & Meyer 2001; Daflon & Cunha 2004). Early studies using OB-type stars found little or no radial metallicity gradient (Fitzsimmons et al. 1990; Kaufer et al. 1994; Kilian-Montenbruck et al. 1994), whereas more recent work shows radial gradients between  $-0.03$  and  $-0.07$  dex  $\text{kpc}^{-1}$  (Gummersbach et al. 1998; Smartt & Rolleston 1997; Rolleston et al. 2000; Daflon & Cunha 2004). Using 69 OB stars in 25 clusters or associations with Galactocentric distances between 4.7 and 13.2 kpc, Daflon et al. (2004) claim a metallicity discontinuity consistent with that found for open clusters and Cepheids. Rolleston et al. (2000), however, see no measurable discontinuity in their sample of about 80 B-type stars from 19 open clusters with Galactocentric radii between 6 and 18 kpc.

Planetary nebula (PN) trace metallicity in the Galactic disk, bulge, and halo. Their ages span 1 to 8 Gyr and thus PNe can in principle probe metallicity with time (Maciel et al. 2003). The difficulty is in separating the different populations and determining accurate distances. One approach is to use Type II PNe (Peimbert 1978) which are disk objects with lower masses that are less likely to be contaminated by nucleosynthetic products from the progenitor star. Radial gradients of the O/H abundance for this population range between  $-0.02$  and  $-0.06$  dex  $\text{kpc}^{-1}$  (Maciel & Quirieza 1999; Henry et al. 2004; Perinotto & Morbidelli 2006). Stanghellini et al. (2006) selected PNe with either elliptical or bipolar core morphologies since they are uniformly distributed in the disk and have more reliable distances. They derived essentially flat gradients. Pottasch & Bernard-Salas (2006) observed both IR and optical transitions to better calculate the ionization correction and therefore derive more accurate abundances. They found a higher radial gradient of  $-0.085$  dex  $\text{kpc}^{-1}$ , although their sample size is only 26 PNe with limited Galactocentric range (3.5 to 9.8 kpc). Maciel et al. (2003) developed a method to determine the age of the PNe central star and reported a flattening of the O/H radial gradient from  $-0.11$  dex  $\text{kpc}^{-1}$  to  $-0.06$  dex  $\text{kpc}^{-1}$  during the last 9 Gyr. Stanghellini & Haywood (2010), however, found the opposite trend: the radial abundance gradients are steepening with time. They used the most up-to-date abundances and distances for 147 PNe, and the Peimbert PNe classification to discriminate age. Henry et al. (2010) analyzed 124 PNe and derived a radial O/H gradient of  $-0.058 \pm 0.006$  dex  $\text{kpc}^{-1}$  between Galactocentric radii 0.9 to 21 kpc with no variation in time. They concluded “From our complete exercise we consider it very likely that the true slope is within the range  $-0.04$  to  $-0.06$  dex  $\text{kpc}^{-1}$ , but we cannot refine the number beyond that point.”

Galactic H II regions are the formation sites of massive OB stars and they reveal the

locations of current Galactic star formation. Their chemical abundances indicate the present state of the interstellar medium and reveal the elemental enrichment caused by the nuclear processing of many stellar generations. Collisionally excited lines are bright in H II regions and provide a sensitive measure of metallicity at optical wavelengths (Pagel 1997). Early studies of O/H radial gradients from optical CELs measured radial gradients from  $-0.04$  to  $-0.13 \text{ dex kpc}^{-1}$  using H II regions with Galactocentric radii of 8 to 14 kpc (Hawley 1978; Peimbert 1978; Talent & Dufour 1979). Using both radio and optical spectroscopy Shaver et al. (1983) significantly expanded the H II region sample and derived an O/H radial gradient of  $-0.07 \pm 0.015 \text{ dex kpc}^{-1}$ . More recent work has focused on the outer Galaxy. Vílchez & Esteban (1996) extended the H II region sample out to  $R_{\text{gal}} = 18 \text{ kpc}$  and found a flatter gradient in the outer Galaxy (also see Fich & Silkey 1991). Deharveng et al. (2000) detected no significant flattening, but measured an overall lower gradient of  $-0.0395 \pm 0.0049 \text{ dex kpc}^{-1}$ .

Observations of CELs in the far infrared (FIR) are less sensitive to extinction by dust and can probe further into the Galactic disk. Unlike their optical counterparts they are not very sensitive to temperature fluctuations; the FIR CELs, however, are weaker and they cannot be used to determine the hydrogen column density (Rudolph et al. 2006). O/H radial gradients in H II regions derived using FIR lines range from  $-0.06$  to  $-0.08 \text{ dex kpc}^{-1}$  (Simpson et al. 1995; Afflerbach et al. 1997; Rudolph et al. 1997). Rudolph et al. (2006) reanalyzed data from 8 studies in a self consistent way and found a vertical shift of 0.25 dex in the O/H ratio between the optical and FIR data that they cannot explain. Moreover, they found no evidence for a flattening of the gradient or a discontinuity in the outer Galaxy.

Large optical telescopes have allowed the detection of optical recombination lines (ORLs) from Galactic H II regions. Unlike CELs, abundance ratios derived from ORLs are not a strong function of temperature fluctuations within the H II region (See §4.3). Using ORLs, Esteban et al. (2005) calculated an O/H radial gradient of  $-0.044 \pm 0.010 \text{ dex kpc}^{-1}$  with a small sample of 8 H II regions with a Galactocentric radius range of 6 to 10 kpc.

Only a decade after their discovery RRLs were used to derive electron temperatures and to indirectly probe metallicity structure in the Galaxy (Churchwell & Walmsley 1975; Churchwell et al. 1978; Mezger et al. 1979; Lichten et al. 1979; Wilson et al. 1979). Converting  $T_e$  values to O/H abundances produced radial gradients between  $-0.04$  and  $-0.06 \text{ dex kpc}^{-1}$ , consistent with both optical and IR observations of the O/H abundance ratio (Wink et al. 1983; Afflerbach et al. 1996; Quireza et al. 2006b).

What do we conclude from these studies? Radial metallicity gradients have been measured to be between 0 and  $-0.1 \text{ dex kpc}^{-1}$ ; to be increasing with time, decreasing with time, or to have no time dependence; to be linear with Galactocentric radius or to have disconti-

nities in the radial profile. The bulk of the data do indicate that the Milky Way disk has a negative radial metallicity gradient, but not much else is very certain.

## 5.2. This Work

A Galactic map of H II region metallicities can inform both Galactic chemical evolution (GCE) models and the merger history of the Milky Way, especially in the outer disk. Using RRLs to derive Galactic metallicity structure has several advantages. RRLs are detected throughout the Galactic disk. Unlike many stellar probes of metallicity, the ISM gas is less likely to suffer from radial mixing on a Galactic scale. It thus preserves the local enrichment history in the disk. H II regions are confined to the thin disk with a scale height of 100 pc, and thus cannot be confused with other Galactic components. Large volumes of gas are sampled and therefore metallicities derived here should not be contaminated by nearby stars.

Using our highest quality data we calculated an O/H radial gradient of  $-0.0446 \pm 0.0049 \text{ dex kpc}^{-1}$ . The observed dispersion in these fits appears to be real and not due to measurement error (also see Shaver et al. 1983; Quireza et al. 2006b). Filtering the sample by Galactic azimuth increases the correlation coefficient and produces gradients between  $-0.03$  and  $-0.07 \text{ dex kpc}^{-1}$ , consistent with the range of values for H II regions in the literature (see §5.1). There is no evidence for non-linear structure or discontinuities in the metallicity distribution with Galactocentric radius when the data are azimuthally averaged.

Twarog et al. (1997) were the first to notice a discontinuity in the radial gradient from observations of iron in open clusters. In Figure 9 we plot  $[\text{Fe}/\text{H}]$  versus  $R_{\text{gal}}$  from their open cluster sample (cf. Figure 3 of Twarog et al.). We explored whether azimuthal metallicity structure could be responsible for the observed discontinuity by filtering their sample into two azimuth ranges:  $330 - 360^\circ$  and  $0 - 30^\circ$  (bottom panels). The metallicity jump near  $R_{\text{gal}} = 10 \text{ kpc}$  is still present for  $\text{Az} = 330 - 360^\circ$ . Given the large range of ages for open clusters, however, any azimuthal structure that existed when the open clusters were formed would confuse the interpretation of the radial gradient. We also filtered their data by Galactic latitude. When open clusters at high Galactic latitudes,  $|b| > 5^\circ$ , are excluded there is no indication of a step in the radial gradient. The open clusters that provided the evidence for such a discontinuity are located between  $10 < R_{\text{gal}} < 12 \text{ kpc}$  and have larger Galactic latitudes.

Observations of Cepheids also reveal azimuthal metallicity structure. The  $[\text{Fe}/\text{H}]$  abundance decreases for sources near  $R_{\text{gal}} \approx 10 \text{ kpc}$  while scanning in Galactic azimuth from Galactic quadrant II to III (Luck et al. 2006; Lemasle et al. 2008; Pedicelli et al. 2009).



There is a similar trend in our RRL electron temperature data (cf., Figure 7 and recall that the metallicity is inversely proportional to the electron temperature). But one should be careful when comparing metallicities in Cepheids with H II regions since they have different ages and may be from a different population. Even though Cepheids are relatively young ( $< 200$  Myr), it only takes the Sun  $\sim 230$  Myr to complete one orbit, whereas H II region abundances probe metallicities at their observed locations. Cepheids are also more likely to be influenced by radial mixing and therefore their current radius may be different than the radius of their birthplace. Pedicelli et al. (2009) claim, however, that the detected metallicity structure from Cepheids was not affected by age or height above the Galactic Plane.

There are reasons to expect that the Galaxy is well-mixed at a given radius. Galactic differential rotation, cloud-cloud collisions, and turbulent diffusion should mix the ISM on time scales of  $10^6$ - $10^9$  yr depending on the mixing mechanism and spatial scale (Roy & Kunth 1995; Scalo & Elmegreen 2004). Local pollution and infalling material, however, can modify these homogeneous abundances. Our H II region RRL results indicate that the gas is not well-mixed in azimuth. We calculate a dispersion of 0.18 dex relative to our linear, radial fit using the Green Bank Sample with QFs of C or better. Observations of the O/H abundance in spiral galaxies measure a dispersion of 0.1 – 0.2 dex at a given radius using the metallicity indicator  $R_{23}$  (Kennicutt & Garnett 1996; van Zee et al. 1998)<sup>6</sup> or the [O III] $\lambda$ 4363 auroral line method (e.g., Rosolowsky & Simon 2008). But it has been shown that this dispersion is consistent with measurement errors (Kennicutt & Garnett 1996; Bresolin 2011). More recent, high quality abundance measurements in spiral galaxies find no evidence of azimuthal structure with a *rms* scatter in the derived abundance gradients on the order of 0.06 dex (Bresolin et al. 2009; Bresolin 2011).

Many GCE models consider chemical evolution along the radial dimension as a function of time and allow for infalling gas (e.g., Matteucci & François 1989; Chiappini et al. 1997; Tosi 1998; Boissier & Prantzos 1999). A key constraint is the radial metallicity gradient as a function of time. Depending on the star formation rate with radius and the composition of infalling material, GCE models can predict a steepening of the metallicity gradient with time (e.g., Tosi 1988; Chiappini et al. 1997), a flattening with time (e.g., Mollà et al. 1997; Hou et al. 2000; Fu et al. 2009), or a constant gradient with time (e.g., Magrini et al. 2009). To our knowledge all such models are axisymmetric and therefore cannot make predictions about metallicity structure along the azimuthal direction.

Chemodynamical models consider both the chemical and dynamical evolution of the

---

<sup>6</sup> $R_{23} = ([\text{O II}]\lambda 3727 + [\text{O III}]\lambda 4959, 5007) / \text{H}\beta$  (Pagel et al. 1979).

Galaxy (e.g., Samland et al. 1997). Some models predict radial metallicity gradients that steepen with time with present-day values of  $\approx -0.07 \text{ dex kpc}^{-1}$  (Samland et al. 1997; Roškar et al. 2008b; Schönrich & Binney 2009). There are several interesting dynamical effects that are important for chemical evolution. Sellwood & Binney (2002) show that radial mixing will result from resonance scattering by spiral arms (also see Roškar et al. 2008a). Schönrich & Binney (2009) developed chemical evolution models that incorporated these radial flows for both stars and gas. These models predict the coevolution of the thick and thin discs without requiring accreted material from outside the Galaxy. Minchev & Famaey (2010) proposed a new mechanism of radial migration involving the resonance overlap of the bar and spiral structure that produced shallower radial metallicity gradients. Samland & Gerhard (2003) model the formation and evolution of a disk galaxy within a growing dark halo using cosmological simulations of structure formation. A bar naturally forms and reduces the radial metallicity gradient in the thin disk to  $-0.02 \text{ dex kpc}^{-1}$ . This is consistent with iron abundances in external galaxies where metallicity gradients are found to be shallower in galaxies with bars (e.g., Vila-Costas & Edmunds 1992). But to our knowledge all of these models do not consider or show results of the chemical evolution in the azimuthal direction.

Many investigators that propose either a discontinuity in the radial gradient or multiple components often use heterogeneous data sets (Vílchez & Esteban 1996; Yong et al. 2005; Luck et al. 2006; Carraro et al. 2007; Lemasle et al. 2008; Sestito et al. 2008; Pedicelli et al. 2009; Andreuzzi et al. 2010). In contrast, studies that use a homogeneous sample and process the data in a self-consistent way typically find linear gradients with no significant discontinuities (Rolleston et al. 2000; Deharveng et al. 2000; Quireza et al. 2006b; Rudolph et al. 2006; Henry et al. 2010). Although here we have combined data from two different telescopes, the GBT and the 140 Foot telescope, the observing technique and data reduction process were identical. Moreover, we get the same results even when using only GBT data. Future efforts should focus on homogeneous samples of a given tracer to reduce systematic errors; for example, the Bologna Open Cluster Chemical Evolution (BOCCE) project (Bragaglia & Tosi 2006).

## 6. Summary

We are discovering H II regions over a wide range of Galactic azimuth in the outer Galaxy (Bania et al. 2010; Anderson et al. 2011). Most metallicity tracers are at optical wavelengths and are restricted to probing the Galactic disk in just the Solar neighborhood near  $Az = 0^\circ$ . Deriving metallicities for this new sample of H II regions will compliment the Apache Point Observatory Galactic Evolution Experiment (APOGEE) that will measure the metallicity of

red giant stars at infrared wavelengths over transgalactic distances (Eisenstein et al. 2011).

Here we have calculated the metallicity of 81 Galactic H II regions using RRLs measured with the GBT. Most of these objects are located between Galactocentric azimuth  $330^\circ$  and  $60^\circ$ . We derived radial metallicity gradients in the range  $-0.03$  to  $-0.07 \text{ dex kpc}^{-1}$ . There is no evidence for any breaks or discontinuities in the radial gradient as probed here by our RRLs observations. We do, however, find evidence for azimuthal structure in the spatial pattern of H II region metallicities, especially in the outer Galactic disk.

D.S.B. thanks Dick Henry for discussions about planetary nebulae and chemical evolution; Anil Pradhan for pointing out recent studies concerning the photoionization cross section of oxygen; and Fred Schwab for providing information about linear regression and metric interpolation. T.M.B. was partially supported by NSF award AST 0707853. LDA was partially supported by SNF and by the NSF through GSSP awards 08-0030 and 09-005 from the NRAO. This research has made use of NASA’s Astrophysics Data System.

## A. Data Reduction and Calibration

### A.1. Averaging Radio Recombination Lines

For hydrogenic recombination line transitions with high principal quantum numbers ( $n > 50$ ), the line parameters of adjacent transitions should be similar. For example, the classical oscillator strength for the H51 $\alpha$  RRL differs from the H50 $\alpha$  RRL by only 2% indicating that these lines should have very similar intensities (Menzel 1968). We averaged the H87 $\alpha$  to H93 $\alpha$  RRLs in order to improve the signal-to-noise ratio of our measurements. Below we discuss the three steps required to average GBT RRL data in this way.

#### A.1.1. Velocity Scale

Because adjacent RRLs are at different frequencies they have different velocity resolutions. Since the H87 $\alpha$  sub-band has the lowest spectral resolution, the spectra are re-gridded to the same velocity scale as the H87 $\alpha$  sub-band. We assume the velocity resolution is constant across the 50 MHz bandwidth. We use a  $\text{Sin}(x)/x$  interpolation to re-grid the spectra of each RRL sub-band onto the H87 $\alpha$  sub-band (e.g., see Balser 2006).

### A.1.2. Velocity Offset

The current GBT system only properly Doppler tracks one RRL sub-band. We used the H89 $\alpha$  sub-band as the Doppler tracked sub-band since it is located near the center of the X-band receiver system. The other RRL sub-bands are Doppler tracked at the sky frequency of the H89 $\alpha$  sub-band. Since Doppler tracking is a function of sky frequency the other RRL sub-bands will be offset, typically by a few channels, relative to the H89 $\alpha$  sub-band. Moreover, since the sky frequency is a function of time the offset will vary slowly in time. The variation in the offset is negligible assuming the data are averaged over time-scales of days and not months.

The relativistic Doppler frequency is given by:

$$\nu_{\text{sky}} = \nu_{\text{rest}} - \nu_{\text{rest}} \frac{1 - V/c}{\sqrt{1 - (V/c)^2}} \quad (\text{A1})$$

where  $\nu_{\text{sky}}$  is the sky frequency,  $\nu_{\text{rest}}$  is the rest frequency,  $V$  is the radial velocity, and  $c$  is the speed of light. The offset is just given by the difference in the derived sky frequency between the RRL sub-band in question and the H89 $\alpha$  sub-band.

### A.1.3. Intensity Scale

Since the telescope’s HPBW varies with RRL sub-band, the line intensities may vary depending on the convolution of the source structure with the telescope’s beam. Assuming a Gaussian telescope beam pattern and a Gaussian source brightness distribution, the relationship between the brightness temperature,  $T_{\text{B}}$ , and the antenna temperature,  $T_{\text{A}}$ , is given by

$$T_{\text{B}} = \frac{T_{\text{A}}}{\eta_{\text{b}}} \left( \frac{\theta_{\text{s}}^2 + \theta_{\text{b}}^2}{\theta_{\text{s}}^2} \right) \quad (\text{A2})$$

where  $\eta_{\text{b}}$  is the beam efficiency,  $\theta_{\text{b}}$  is the FWHM beam size, and  $\theta_{\text{s}}$  is the angular source size. Observations of a source with a brightness temperature  $T_{\text{B}}$  and size  $\theta_{\text{s}}$  with two different Gaussian beams  $\theta_{\text{b}}(1)$  and  $\theta_{\text{b}}(2)$  will produce antenna temperatures  $T_{\text{A}}(1)$  and  $T_{\text{A}}(2)$  that are related by

$$T_{\text{A}}(1) = \frac{T_{\text{A}}(2) [\theta_{\text{obs}}(1)^2 - \theta_{\text{b}}(1)^2 + \theta_{\text{b}}(2)^2]}{\theta_{\text{obs}}(1)^2} \quad (\text{A3})$$

where  $\theta_{\text{obs}}(1)$  is the observed (convolved) source size for beam 1  $\theta_{\text{obs}}(1)^2 = \theta_{\text{s}}^2 + \theta_{\text{b}}(1)^2$ . If the source is larger than the beam size,  $\theta_{\text{obs}}(1) \gg \theta_{\text{b}}(1)$ , then  $T_{\text{A}}(1) = T_{\text{A}}(2)$ , whereas if the source size is much smaller than the beam size,  $\theta_{\text{obs}}(1) \approx \theta_{\text{b}}(1)$ , then  $T_{\text{A}}(1) = T_{\text{A}}(2)(\theta_{\text{b}}(2)/\theta_{\text{b}}(1))^2$ .

The continuum data were observed centered at 8665 GHz with a bandwidth of 320 MHz. The H91 $\alpha$  transition lies within this observed band. We therefore scaled the line intensity of the other RRL transitions to the H91 $\alpha$  transition using Equation A3. In principle any flux density calibration should cancel when calculating the line-to-continuum ratio but since we only have a continuum measurement near one RRL this is not true when the RRLs are averaged. Any atmospheric or gain fluctuations should be approximately constant across the 8 to 10 GHz range of our measurements; they should not cause any significant error in determining the line-to-continuum ratio.

## A.2. Flux Density Calibration

During both the line and continuum observations a noise diode was used to inject a calibration signal with an intensity of about 5–10% of the nominal total system temperature. The noise diodes have been calibrated in the laboratory with 50 MHz resolution to about 10% accuracy. For the X-band receiver system the noise diodes are  $T_{\text{cal}} \approx 2$  K.

Astronomical calibration sources can be used to validate or revise the  $T_{\text{cal}}$  values, whereby a correction factor, CF, the ratio of the expected intensity to the measured intensity, is derived. Below we explore several different calibration methods. We assume a telescope gain of  $2 \text{ K Jy}^{-1}$  (Ghigo et al. 2001) and the flux densities from Peng et al. (2000). We neglect corrections due to opacity and elevation gain because the former are typically a few percent under most conditions and the latter are less than 5% at 10 GHz.

### A.2.1. Flux continuum calibrator with the Digital Continuum Receiver (DCR)

DCR measurements of the flux density calibrator 3C147 were used to derive correction factors. The DCR was configured to center an 80 MHz bandwidth at each RRL sub-band frequency, and a 320 MHz bandwidth at the continuum band frequency of 8665 MHz. The spectral line data had bandwidths of 50 MHz, but the nearest available filter to this bandwidth was 80 MHz. We assume that the true calibration does not significantly vary across the 50 MHz RRL sub-bands.

Observations of 3C147 were taken near transit on 6 January 2008, 20 February 2008, and 22 February 2008. The weather was not optimal for these observations although the conditions were best on 6 January 2008 (see Table 7). For this epoch the correction factors are typically less than 10%, consistent with the expected accuracy of the laboratory  $T_{\text{cal}}$  measurements. The intensity of 3C147 varies by about 1–2% between the 80 MHz and 320

MHz bandwidth observations centered at similar frequencies.

Given the marginal weather conditions we did not apply these CF’s to the data. The primary goal here, moreover, is to calculate electron temperatures which are a function of the line-to-continuum ratio (c.f., Equation 1). Since many errors cancel when taking the ratio of these intensities only a relative calibration is required.

### *A.2.2. Flux continuum calibrator with the Auto-correlation Spectrometer (ACS)*

The flux density calibrator 3C147 was also observed using the ACS in the same configuration as for the RRL measurements. From these data  $T_{\text{cal}}$  values were calculated for each spectral channel with the same spectral resolution. The  $T_{\text{cal}}$  vector may be used not only as a flux density calibration but also to produce a bandpass calibration, since the frequency structure of 3C147 is known (Johnson et al. 2002; Pisano et al. 2007).

There are significant disadvantages of using a vector  $T_{\text{cal}}$  calibration for our data. Any gain fluctuations (e.g., weather) are not very easy to subtract since a baseline cannot be determined as with the DCR data. Also, if the  $T_{\text{cal}}$  values are applied to the data they will add noise to the spectrum. We therefore did not pursue this calibration method.

### *A.2.3. Flux line calibrator with the ACS*

If a spectral line of known flux density is within the RRL sub-band then it can be used to calculate the  $T_{\text{cal}}$  value near this frequency. Since there are not many spectral lines with known flux densities this method is typically not feasible. Yet, any stable spectral line with a high signal-to-noise ratio and well behaved spectral baselines can provide a relative calibration. For our observations the RRL itself, if sufficiently bright, can be used as a relative flux calibrator.

For example, Quireza et al. (2006b) used the H II region W3 to measure a relative intensity calibration scale for two adjacent RRLs. Here we use all target sources in our sample with a continuum intensity greater than 5 K to determine an average relative calibration. This calibration will average over variations in the spectral baselines, weather, elevation gain, etc.

Let  $H91$ ,  $IH91$ , and  $AH91$  denote the  $H91\alpha$  intensity, the interpolated  $H91\alpha$  intensity, and the averaged RRL intensity scaled to the  $H91\alpha$  frequency as discussed above. Figure 10 plots RRL intensity ratios for both circular polarizations for all sources with a continuum

intensity larger than 5 K. Shown are the RRL intensity ratios H91/IH91 and H91/AH91 for each polarization. We excluded the H90 $\alpha$  RRL sub-band since it was difficult to determine a good baseline near the carbon RRL due to nearby higher order RRLs. We calculated ratios of  $1.002 \pm 0.0067$  for H91/IH91 (LL);  $1.003 \pm 0.0063$  for H91/IH91 (RR);  $1.056 \pm 0.0197$  for H91/AH91 (LL); and  $1.005 \pm 0.0159$  for H91/AH91 (RR). To within the uncertainty the H91 and IH91 intensities are identical—this should be the case if the interpolation is done properly. There is a measurable systematic offset when comparing the H91/AH91 ratios, however, that should stem from errors in the  $T_{\text{cal}}$  values and any systematic errors in our averaging technique. These offsets are less than 5%. There is no systematic effect of these ratios with respect to either the continuum intensity or angular size. The dispersion in H91/AH91 is a result of fitting spectral baselines and Gaussian profiles, random noise, weather fluctuations, elevation gain fluctuations, etc. It is therefore a good measure of the uncertainties in our observing and data analysis procedures.

Figure 11 plots the RRL polarization ratios, LL/RR, for H91, IH91, and AH91. We calculate polarization ratios of  $1.027 \pm 0.0101$  for H91;  $1.028 \pm 0.0105$  for IH91; and  $0.978 \pm 0.0043$  for AH91. The polarization ratios are also not a function of either the continuum intensity or angular size. The H91 polarization ratios are about 3% from unity, well within the expected  $T_{\text{cal}}$  uncertainties of 10%. The polarization ratios for the other RRLs show similar results. To within the uncertainty the H91 and IH91 polarizations ratios are identical, again as expected. The AH91 polarization ratios are within 2% of unity, consistent with random errors in  $T_{\text{cal}}$ . That is, if the errors in determining  $T_{\text{cal}}$  are random they should average to unity given enough RRL sub-bands. Moreover, the dispersion in the distribution should decrease as  $1/\sqrt{N}$ . From Figure 11 we see a decrease in the dispersion from 0.0101 to 0.0043 when we compare the single sub-band H91 to the averaged AH91. This is consistent with the six RRL sub-bands used in the average.

Based on the H91/AH91 ratios for each polarization we derived and applied corrections factors of  $\text{CF} = 1.056 \pm 0.0197$  for LL and  $\text{CF} = 1.005 \pm 0.0159$  for RR. Overall we deem that the relative calibration scale is accurate to within 5%.

## B. Accuracy of the Electron Temperature Derivation

We estimate the accuracy of our derived electron temperatures by calculating both measurement and calibration errors. The measurement errors are listed in Table 1 and were calculated by propagating the uncertainty in the hydrogen and helium RRL line intensity and width, together with the continuum intensity uncertainty. The average measurement error is  $1.6\% \pm 1.1\%$  with respect to the electron temperature. The calibration errors are

estimated to be  $< 5\%$  (see §A.2). The accuracy of our electron temperatures should therefore be  $\sim 5\%$  or better. This does not include systematic errors which are difficult to determine. If we could estimate any systematic error we would remove it! Our sources, however, were selected to minimize potential systematic errors. For example, determining the baseline or zero level for the continuum intensity is one potential source of systematic error. This is particularly difficult for sources located in complex regions where extended emission often exists in the baseline region. For such cases our data analysis procedures will systematically underestimate the continuum intensity and therefore the electron temperature. We have carefully chosen sources that are well isolated to minimize such systematic effects.

*Facility:* GBT

## REFERENCES

- Afflerbach, A., Churchwell, E., Acord, J. M., Hofner, P., Kurtz, S., & De Pree, C. G. 1996, *ApJS*, 106, 423
- Afflerbach, A., Churchwell, E., Werner, M. W. 1997, *ApJ*, 478, 190
- Anderson, L. D., & Bania, T. M. 2009, *ApJ*, 690, 706
- Anderson, L. D., Bania, T. M., Balser, D. S., & Rood, R. T. 2011, *ApJ*, in press
- Andreuzzi, G. Bragaglia, A., Tos, M., & Marconi, G. 2010, *MNRAS*, 412, 1265
- Andrievsky, S. M., Kovtyukh, V. V., Luck, R. E., Lépine, J. R. D., Maciel, W. J., & Beletsky, Y. V. 2002, *A&A*, 392, 491
- Andrievsky, S. M., Luck, R. E., Martin, P., & Lépine, J. R. D., 2004, *A&A*, 413, 159
- Audouze, J. & Tinsley, B. M. 1976, *ARA&A*, 14, 43
- Baldwin, J. A., Ferland, G. J., Martin, P. G., Corbin, M. R., Cota, S. A., Peterson, B. M., & Slettebak, A. 1991, *ApJ*, 374, 580
- Balser, D. S. 1995, Ph.D. Thesis, Boston Univ. (see <http://find.nrao.edu/theses>.)
- Balser, D. S. 2006, *AJ*, 132, 2326
- Bania, T. M., Anderson, L. D., Balser, D. S., & Rood, R. T. 2010, *ApJ*, 718, L106
- Bania, T. M., Balser, D. S., Rood, R. T., Wilson, T. L., & Wilson, T. A. 1997, *ApJS*, 113, 353



- Blitz, L., Fich, M., & Stark, A. A. 1982, *ApJS*, 49, 183
- Boesgaard, A. M., & Steigman, G., 1985, *ARA&A*, 23, 319
- Boissier, S., & Prantzos, N. 1999, *MNRAS*, 307, 857
- Bragaglia, A., & Tosi, M. 2006, *AJ*, 131, 1544
- Brand, J. 1986, PhD Thesis, Leiden Univ. (Netherlands)
- Brand, J., & Wouterloot, J. G. A. 2007, *A&A*, 464, 909
- Bresolin, F. 2011, *ApJ*, 730, 129
- Bresolin, F., Gieren, W., Kudritzki, R.-P., Pietrzyński, G., Urbaneja, M. A., & Carraro, G. 2009, *ApJ*, 700, 309
- Caputo, F., Marconi, M., Musella, I., Pont, F. 2001, *A&A*, 372, 544
- Carigi, L., Peimbert, M., Esteban, C., & García-Rojas 2005, *ApJ*, 623, 213
- Carraro, G., Geisler, D., Villanova, S., Frinchaboy, P. M., & Majewski, S. R. 2007, *A&A*, 476, 217
- Chen, L., Hou, J. L., & Wang, J. J. 2003, *AJ*, 125, 1397
- Chiappini, C., Matteucci, F., & Gratton, R. 1997, *ApJ*, 477, 765
- Churchwell, E., Smith, L. F., Mathis, J., Mezger, P. G., & Huchtmeier, W. 1978, *A&A*, 70, 719
- Churchwell, E., & Walmsley, C. M. 1975, *A&A*, 38, 451
- Colavitti, E., Matteucci, F., & Murante, G. 2008, *A&A*, 483, 401
- Dafon, S., & Cunha, K. 2004, *ApJ*, 617, 1115
- Dafon, S., Cunha, K., & Butler, K. 2004, *ApJ*, 606, 519
- Deharveng, L., Peña, M., Caplan, J., & Costero, R. 2000, *MNRAS*, 311, 329
- Digel, S., De Geus, E., & Thaddeus, P. 1994, *ApJ*, 422, 92
- Efron, B. 1979, *SIAM*, 21, 460
- Eisenstein, D. J., et al. 2011, arXiv:1101.1529

- Esteban, C., García-Rojas, J., Peimbert, M. Peimbert, A., Ruiz, M. T., Rodríguez, & Carigi, L. 2005, *ApJ*, 618, L95
- Feigelson, E. D., & Babu, G. J. 1992, *ApJ*, 397, 55
- Felli, M., & Churchwell, E. 1972, *A&AS*, 5, 369
- Felli, M., Harten, R. H., Habing, H. J., & Israel, F. P. 1978, *A&AS*, 32, 423
- Fich, M., Blitz, L., & Stark, A. A. 1989, *ApJ*, 342, 272
- Fich, M., & Silkey, M. 1991, *ApJ*, 366, 107
- Fish, V. L., Reid, M. J., Wilner, D. J., & Churchwell, E. 2003, *ApJ*, 587, 701
- Fitzsimmons, A., Brown, P. J. F., Dufton, P. L., & Lennon, D. J. 1990, *A&A*, 232, 437
- Friel, E. D. 1995, *ARA&A*, 33, 381
- Friel, E. D., Janes, K. A., Tavares, M., Scott, J., Katsanis, R., Lotz, J., Hong, L., & Miller, N. 2002, *AJ*, 124, 2693
- Fu, J., Hou, J. L., Yin, J., Chang, R. X. 2009, *ApJ*, 696, 668
- Garay, G., & Rodríguez, L. F. 1983, *ApJ*, 266, 263
- García-Rojas, J., & Esteban, C. 2007, *ApJ*, 670, 457
- García-Rojas, J., Esteban, C., Peimbert, A., Rodríguez, M., Peimbert, M., & Ruiz, M. T. 2007, *Rev. Mex. AA*, 43, 3
- Ghigo, F., Maddalena, R., Balsa, D., & Langston, G. 2001, *GBT Commissioning Memo 10*
- Gordon, M. A., 1976, in *Methods of Experimental Physics. Vol. 12. Astrophysics. Part C: Radio observations*, 277
- Gordon, W. J., & Wixom, J. A. 1978, *Mathematics of Computation*, 32, 253
- Gummersbach, C. A., Kaufer, A., Schäfer, D. R., Szeifert, T., & Wolf, B., 1998, *A&A*, 338, 881
- Hawley, S. A. 1978, *ApJ*, 224, 417
- Henry, R. B. C., Kwitter, K. B., & Balick, B. 2004, *ApJ*, 127, 2284

- Henry, R. B. C., Kwitter, K. B., Jaskot, A. E., Balick, B., Morrison, M. A., & Milingo, J. B. 2010, *ApJ*, 724, 748
- Henry, R. B. C., & Worthey, G. 1999, *PASP*, 111, 919
- Hou, J. L., Prantzos, N., & Boissier, S. 2000, *A&A*, 362, 921
- Isobe, T., Feigelson, E. D., Akritas, M. G., & Babu, G. J. 1990, *ApJ*, 364, 104
- Janes, K. A. 1979, *ApJS*, 39, 135
- Johnson, C., Maddalena, R., Ghigo, F., & Balser, D. 2002, GBT Commissioning Memo 22
- Kaufers, A., Szeifert, Th., Krenzin, R., Baschek, B., & Wolf, B. 1994, *A&A*, 289, 740
- Kennicutt, R. C., & Garnett, D. R. 1996, *ApJ*, 456, 504
- Kilian-Montenbruck, J., Gehren, T., & Nissen, P. E. 1994, *A&A*, 291, 757
- King, I. R. 1971, *PASP*, 83, 377
- Kuchar, T. A. & Bania, T. M. 1994, *ApJ*, 436, 117
- Kolpak, M. A., Jackson, J. M., Bania, T. M., & Clemens, D. P. 2003, *ApJ*, 582, 756
- Lemasle, B., François, P., Piersimoni, A., Pedicelli, S., Bono, G., Laney, D., Primas, F., & Romaniello, M. 2008, *A&A*, 490, 613
- Lichten, S. M., Rodriguez, L. F., & Chaisson, E. J. 1979, *ApJ*, 229, 524
- Liu, X.-W., Storey, P. J., Barlow, M. J., Danziger, I. J., Cohen, M., & Bryce, M. 2000, *MNRAS*, 312, 585
- Lockman, F. J. 1989, *ApJS*, 71, 469
- Lockman, F. J., Pisano, D. J., & Howard, G. J., 1996, *ApJ*, 472, 173
- Luck, R. E., Gieren, W. P., Andrievsky, S. M., Kovtyukh, V. V., Fouqué, P., Pont, F., & Kienzle, F. 2003, *A&A*, 401, 939
- Luck, R. E., Kovtyukh, V. V., & Andrievsky, S. M. 2006, *AJ*, 132, 902
- Mathis, J. S. 1986, *PASP*, 98, 995
- Maciel, W. J., Costa, R. D. D., & Uchida, M. M. M. 2003, *A&A*, 397, 667

- Maciel, W. J., & Quireza, C. 1999, *A&A*, 345, 629
- Magrini, L., Sestito, P., Randich, S., & Galli, D. 2009, *A&A*, 494, 95
- Markwardt, C. B. 2009, *Astronomical Data Analysis Software and Systems XVIII* (ASP Conf. Ser. 411), ed. D. A. Bohlender, D. Durand, & P. Dowler (San Francisco, CA: ASP), 251
- Matteucci, F., & , Franoi, P. 1989, *MNRAS*, 239, 885
- Menten, K. M., Reid, M. J., Forbrich, J., & Brunthaler, A. 2007, *A&A*, 474, 515
- Menzel, D. H. 1968, *Nature*, 218, 756
- Mezger, P. G., Pankonin, V., Schmid-Burgk, J., Thum, C., & Wink, J. 1979, *A&A*, 80, L3
- Minchev, I., & Famaey, B. 2010, *ApJ*, 722, 112
- Moll, M., Ferrini, F., & Diaz, A. I. 1997, *ApJ*, 475, 519
- Nahar, S. N., Montenegro, M., Eissner, W., & Pradhan, A., K. 2010, *Physical Review A*, 82, 5401
- Oliveira, S., & Maciel, W. J. 1986, *Ap&SS*, 128, 421
- Pagel, B. E. J., Edmunds, M. G., Blackwell, D. E., Chun, M. S., & Smith, G. 1979, *MNRAS*, 189, 95
- Pagel, B. E. J. 1997, *Nucleosynthesis and Chemical Evolution of Galaxies* (Cambridge: Cambridge University Press)
- Pagel, B. E. J., & Edmunds, M. G. 1981, *ARA&A*, 19, 77
- Pedicelli, S., Bono, G., Lemasle, B., Franois, P., Groenewegen, M., Lub, J., Pel, J. W., Laney, D., Piersimoni, A., Romaniello, M., Buonanno, R., Caputo, F., Cassisi, S., Castelli, F., Leurini, S., Pietrinferni, A., Primas, F., & Pritchard, J. 2009, *A&A*, 504, 81
- Peimbert, M. 1975, *ARA&A*, 13, 113
- Peimbert M., 1978, in *IAU Symp. 76, Planetary Nebulae*, ed. Y. Terzian (Reidel: Dordrecht), 215
- Peimbert, A., & Peimbert, M. 2010, *ApJ*, 724, 791

- Peng, B., Kraus, A., Krichbaum, T. P., & Witzel, A. 2000, *A&AS*, 145, 1
- Pilyugin, L. S., Ferrini, F., & Shkvarun, R. V. 2003, *A&A*, 401, 557
- Pisano, D.J., Maddalena, R., Figura, C., & Wagg, J. 2007, GBT Memo 246
- Perinotto, M., & Morbidelli, L. 2006, *MNRAS*, 372, 45
- Pottasch, S. R., & Bernard-Salas, J., 2006, *A&A*, 457, 189
- Prantzos, N. 2003, *Rev. Mex. AA*, 17, 121
- Quiroza. C., Rood, R. T., Balser, D. S., & Bania, T. M. 2006a, *ApJS*, 165, 338
- Quiroza. C., Rood, R. T., Bania, T. M., Balser, D. S., & Maciel, W. J. 2006b, *ApJ*, 653, 1126
- Reid, M. J., Menten, K. M., Brunthaler, A., Zheng, X. W., Moscadelli, L., & Xu, Y. 2009, *ApJ*, 693, 397
- Roelfsema, P. R., Goss, W. M., & Mallik, D. C., V. 1992, *ApJ*, 394, 188
- Rolleston, W. R. J., Smartt, S. J., Dufton, P. L., & Ryans, R. S. I. 2000, *A&A*, 363, 537
- Rosolowsky, E., & Simon, J. D. 2008, *ApJ*, 675, 1213
- Roškar, R., Debattista, Stinson, G. S., V. P., Quinn, T. R., Kaufmann, T., & Wadsley, J. 2008, *ApJ*, 675, L65
- Roškar, R., Debattista, V. P., Quinn, T. R., Stinson, G. S., & Wadsley, J. *ApJ*, 684, L79
- Roy, J.-R., & Kunth, D. 1995, *A&A*, 294, 432
- Rubin, R. H. 1985, *ApJS*, 57, 349
- Rubin, V. C., Kumar, C. K., & Ford, W. K., Jr. 1972, *ApJ*, 177, 31
- Rudolph, A. L., Brand, J., De Geus, E. J., & Wouterloot, J. G. A. 1996, *ApJ*, 458
- Rudolph, A. L., Fich, M., Bell, G. R., Norsen, T., Simson, J. P., Haas, M. R., & Erickson, E. F. 2006, *ApJS*, 162, 346
- Rudolph, A. L., Simson, J. P., Haas, M. R., Erickson, E. F., & Fich, M. 1997, *ApJ*, 489, 94
- Samland, M., & Gerhard, O. E. 2003, *A&A*, 399, 961

- Samland, M., Hensler, G., & Theis, Ch. 1997, *ApJ*, 476, 544
- Scalo, J., & Elmegreen, B. G. 2004, *ARA&A*, 42, 275
- Schönrich, R., & Binney, J. 2009, *MNRAS*, 396, 203
- Searle, L. 1971, *ApJ*, 168, 327
- Sellwood, J. A., & Binney, J. J. 2002, *MNRAS*, 336, 785
- Sestito, P., Bragaglia, A., Randich, S., Pallavicini, R., Andrievsky, S. M., & Korotin, S. A. 2008, *A&A*, 488, 943
- Shaver, P. A., McGee, R. X., Newton, L. M., Danks, A. C., & Pottasch, S. R. 1983, *MNRAS*, 204, 53
- Shepard, D. 1968, *Proc. 1968 ACM Nat. Conf.*, 517
- Shields, J. C., & Kennicutt, Jr. R. C., 1995, *ApJ*, 454, 807
- Simpson, J. P., Colgan, S. W. J., Rubin, R. H., Erickson, E. F., & Haas, M. R. 1995, *ApJ*, 444, 721
- Smartt, S. J., & Rolleston, W. R. 1997, *ApJ*, 481, L47
- Smith, H. E. 1975, *ApJ*, 199, 591
- Sofia, U. J., & Meyer, D. M. 2001, *ApJ*, 554, L221
- Stanghellini, L., Guerrero, M. A., Cunha, K., Manchado, A., & Villaver, E. 2006, *ApJ*, 651, 898
- Stanghellini, L., & Haywood, M. 2010
- Steigman, G. 2007, *Annu. Rev. Nucl. Part. Sci.*, 57, 463
- Stil, J. M., Taylor, A. R., Dickey, J. M., Kavars, D. W., Martin, P. G., Rothwell, T. A., Boothroyd, A. I., Lockman, F. J., & McClure-Griffiths, N. M., *AJ*, 132, 1158
- Talent, D. L., & Dufour, R. J. 1979, *ApJ*, 233, 888
- Tosi M. 1988, *A&A*, 197, 33
- Tosi M. 1998, in *Nuclei and their Galactic Evolution*, eds. N. Prantzos, M. Tosi, & R. von Steiger (Dordrecht: Kluwer), 207

- Tosi, M. 2000, in *The Evolution of the Milky Way*, ed. F. Matteucci & F. Giovannelli (Dordrecht: Kluwer), 505
- Trimble, V. 1975, *Rev. Mod. Physics*, 47, 877
- Twarog, B. A., Ashman, K. M., & Anthony-Twarog, B. J. 1997, *AJ*, 114, 2556
- van den Bergh, S. 1974, *ARA&A*, 13, 217
- van Zee, L., Salzer, J. J., Haynes, M. P., O’Donoghue, A. A., & Balonek, T. J. 1998, *AJ*, 116, 2805
- Vila-Costas, M. B., & Edmunds, M. G. 1992, *MNRAS*, 259, 121
- Vílchez, J. M., & Esteban, C. 1996, *MNRAS*, 280, 720
- von Procházka, A. A., Remijan, A. J., Balsler, D. S., Ryans, R. S. I., Marshall, A. H., Schwab, F. R., Hollis, J. M., Jewell, P. R., & Lovas, F. J. 2010, *PASP*, 122, 354
- Wilson, T. L., Bieging, J., & Wilson, W. E. 1979, *A&A*, 71, 205
- Wilson, T. L., & Rood, R. T. 1994, *ARA&A*, 32, 191
- Wink, J. E., Wilson, T. L., & Bieging, J. H. 1983, *A&A*, 127, 211
- Yong, D., Carney, B., & Teixeira de Almeida, M. L. 2005, *AJ*, 130, 597
- Yong, D., Carney, B., Teixeira de Almeida, M. L., & Pohl, B. L. 2006, *AJ*, 131, 2256

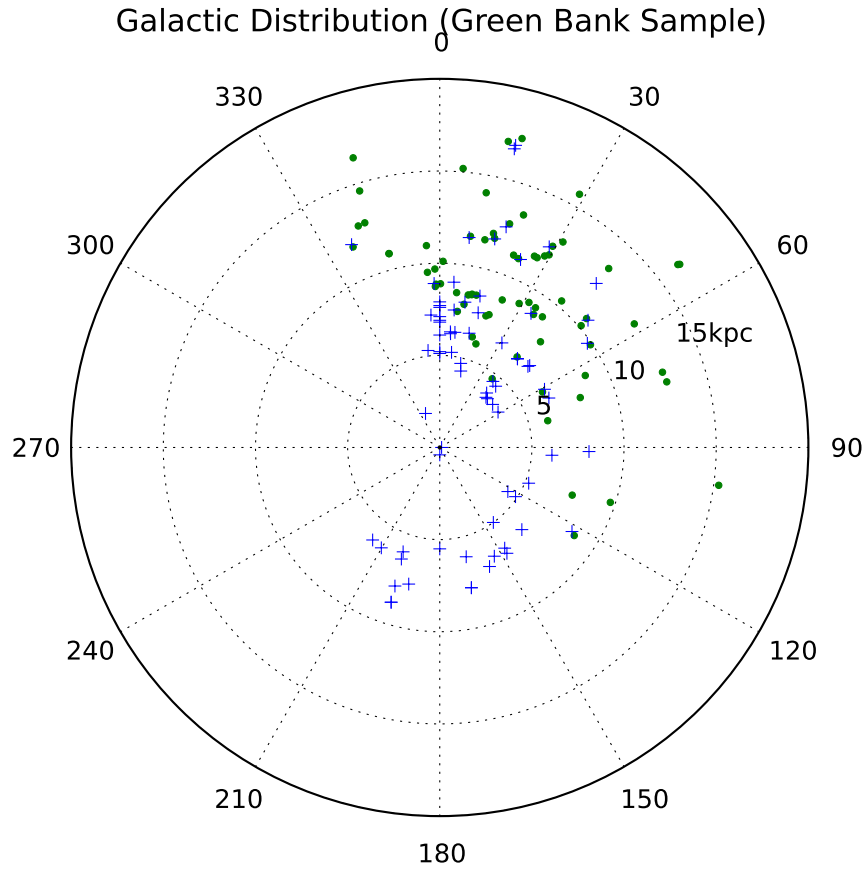


Fig. 1.— H II region survey Galactic distribution ( $l, R_{\text{gal}}$ ). Shown are the H II regions from the GBT (green points) and 140 Foot telescope (blue crosses) surveys. Only quality factor values of C and better are included (see §4).



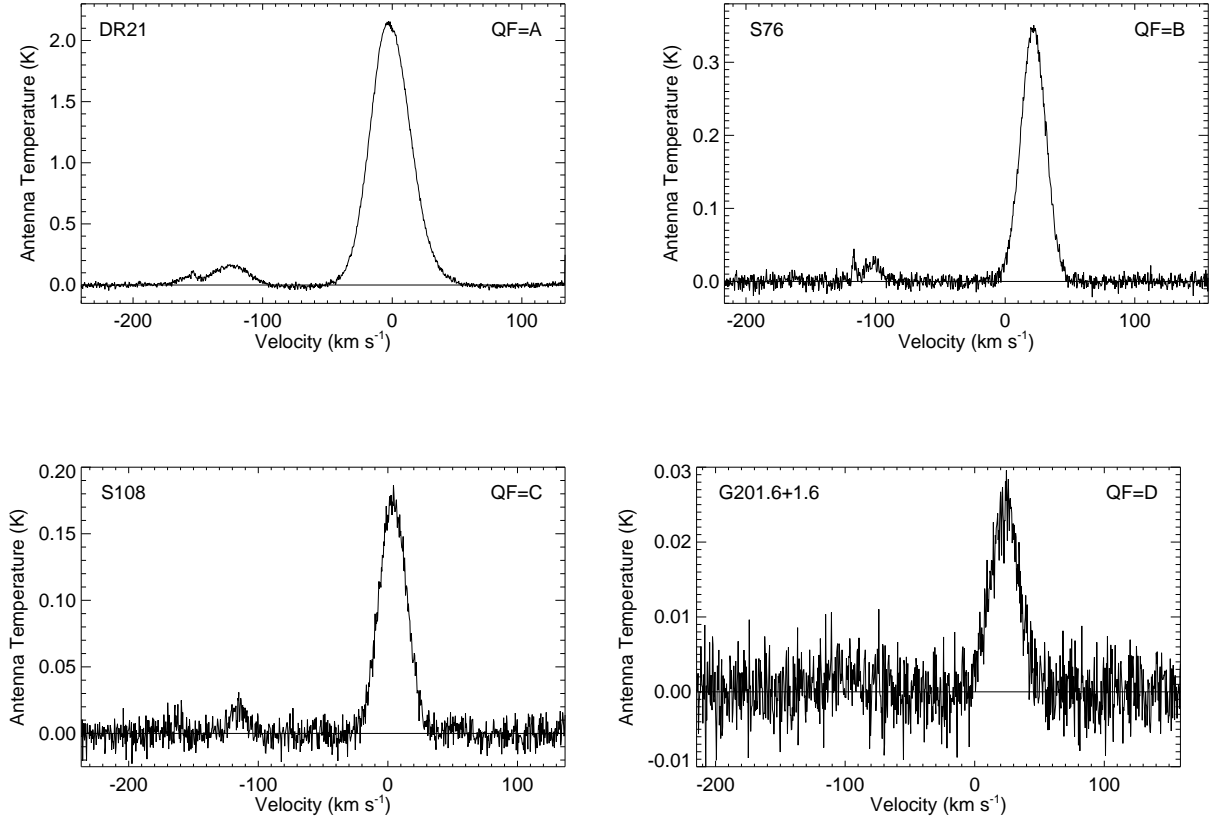


Fig. 2.— Sample H II region RRL spectra. The antenna temperature is plotted as a function of the LSR velocity. The LSR velocity is referenced with respect to the H89 $\alpha$  RRL. For some sources the He and C RRLs, located about  $-125 \text{ km s}^{-1}$  from the H line, were detected. A third or fourth order polynomial function was fitted to the line free regions and removed from the data. The quality factor is shown at the top right-hand corner of each plot, where QF=A is excellent and QF=D is poor.

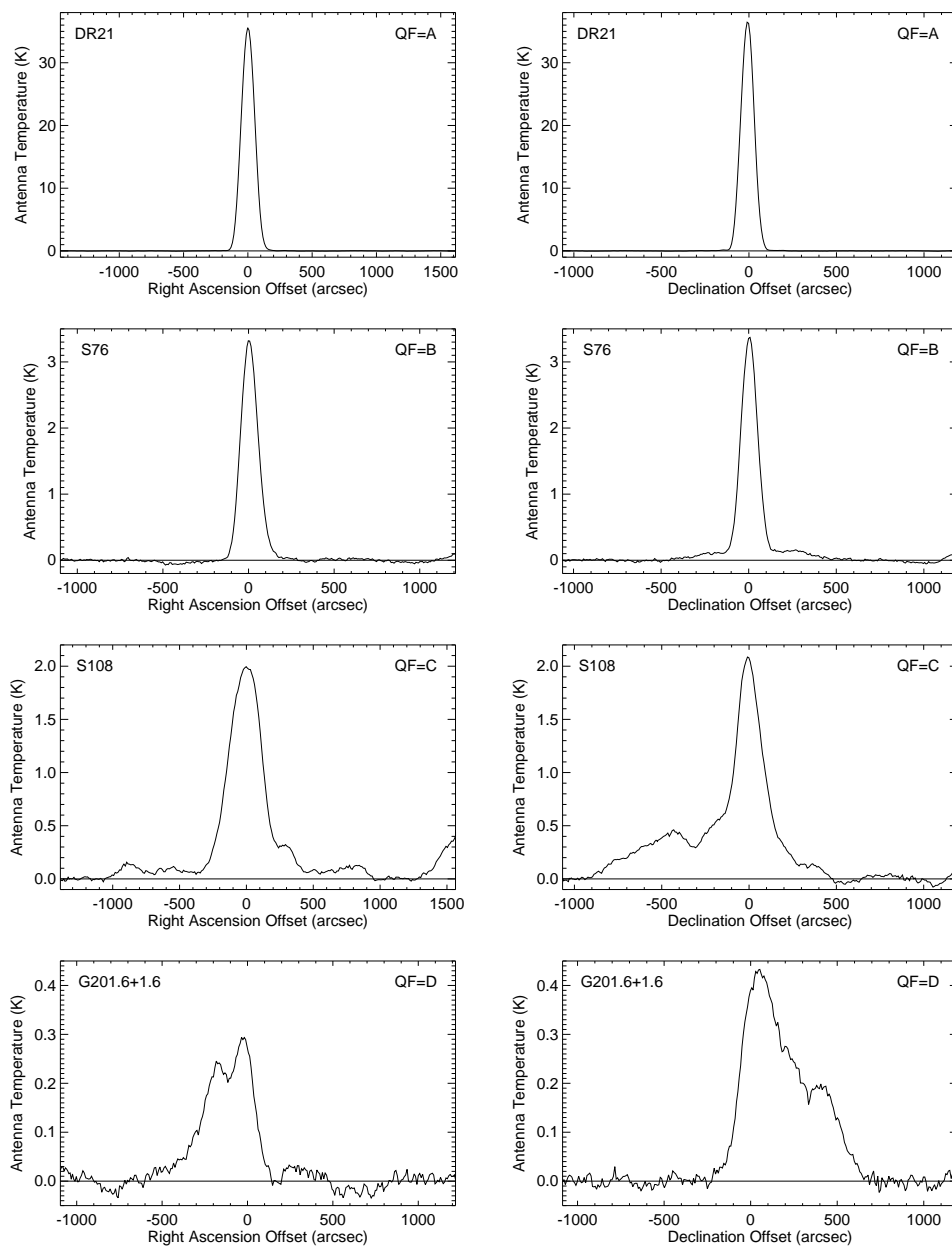


Fig. 3.— Continuum scans for the Figure 2 H II regions. The antenna temperature is plotted as a function of the offset position relative to the target coordinates listed in Table 1. For each source the R.A. and Decl. scans are shown. A third or fourth order polynomial function was fitted to the baseline and removed from the data. The quality factor is shown at the top right-hand corner of each plot, where QF=A is excellent and QF=D is poor.

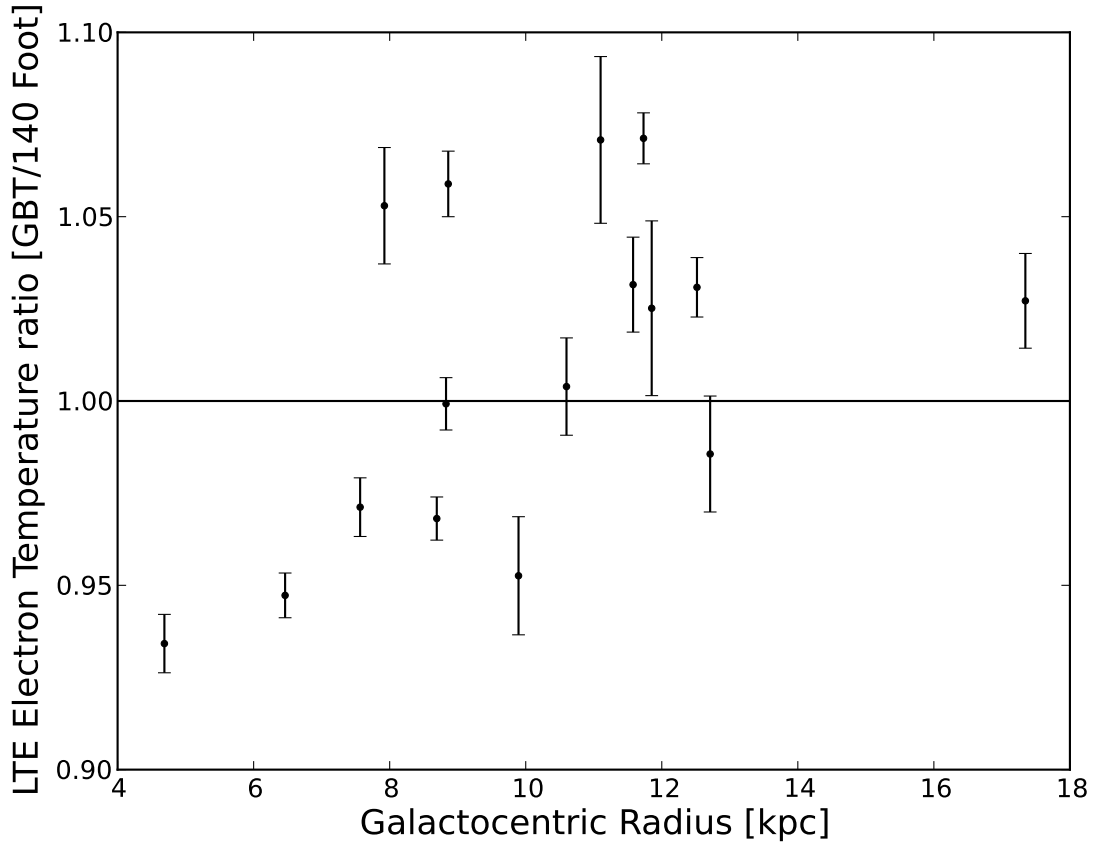


Fig. 4.— LTE electron temperature ratio (GBT/140 Foot) for sources in common between the GBT and 140 Foot telescope samples. Only quality factor values of C and better for both line and continuum data are included. A least-squares fit to the data ( $y = ax + b$ ) yields:  $a = 0.932 \pm 0.045$  and  $b = 0.0075 \pm 0.0043$ .

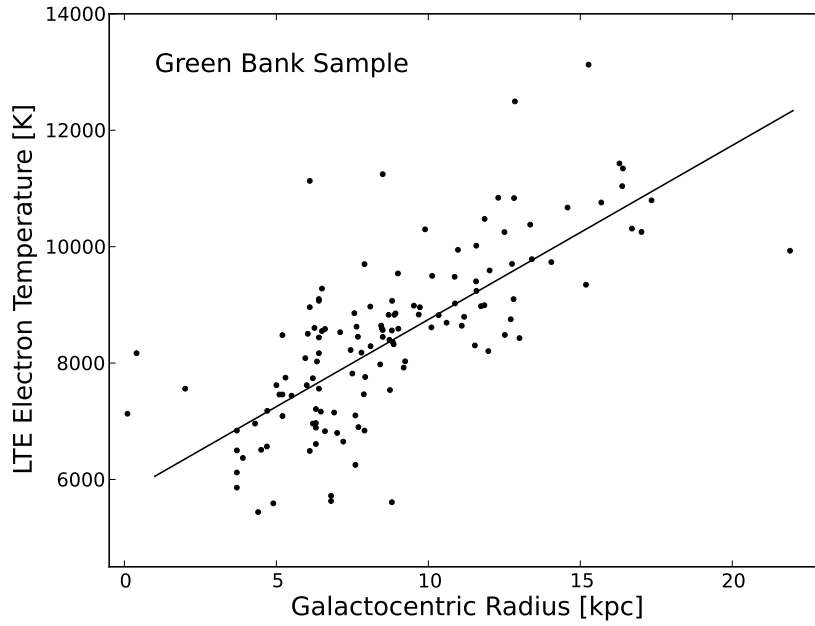
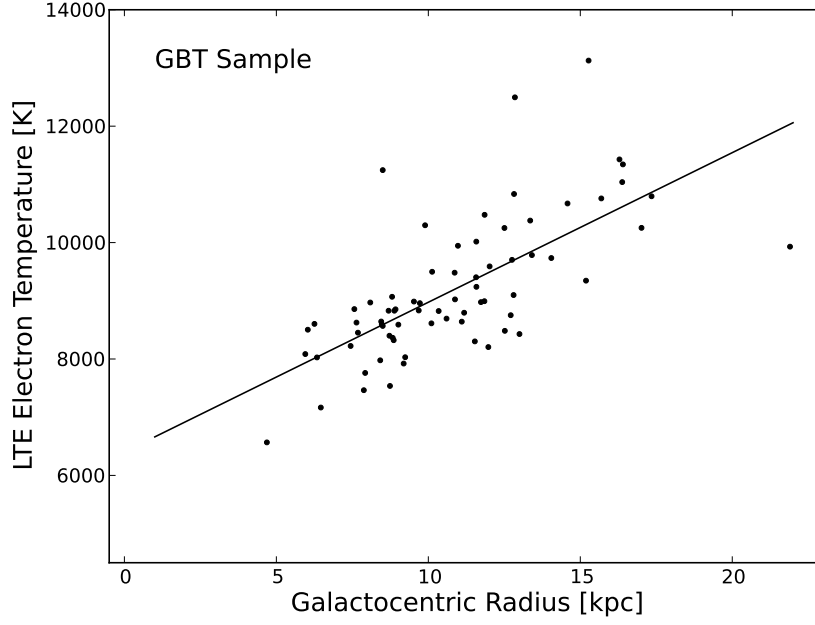


Fig. 5.— Electron temperature radial gradient for the GBT Sample (top) and the Green Bank Sample (bottom). Only quality factor values of C and better for both line and continuum data are included. The solid line is a linear least-squares fit to the data.

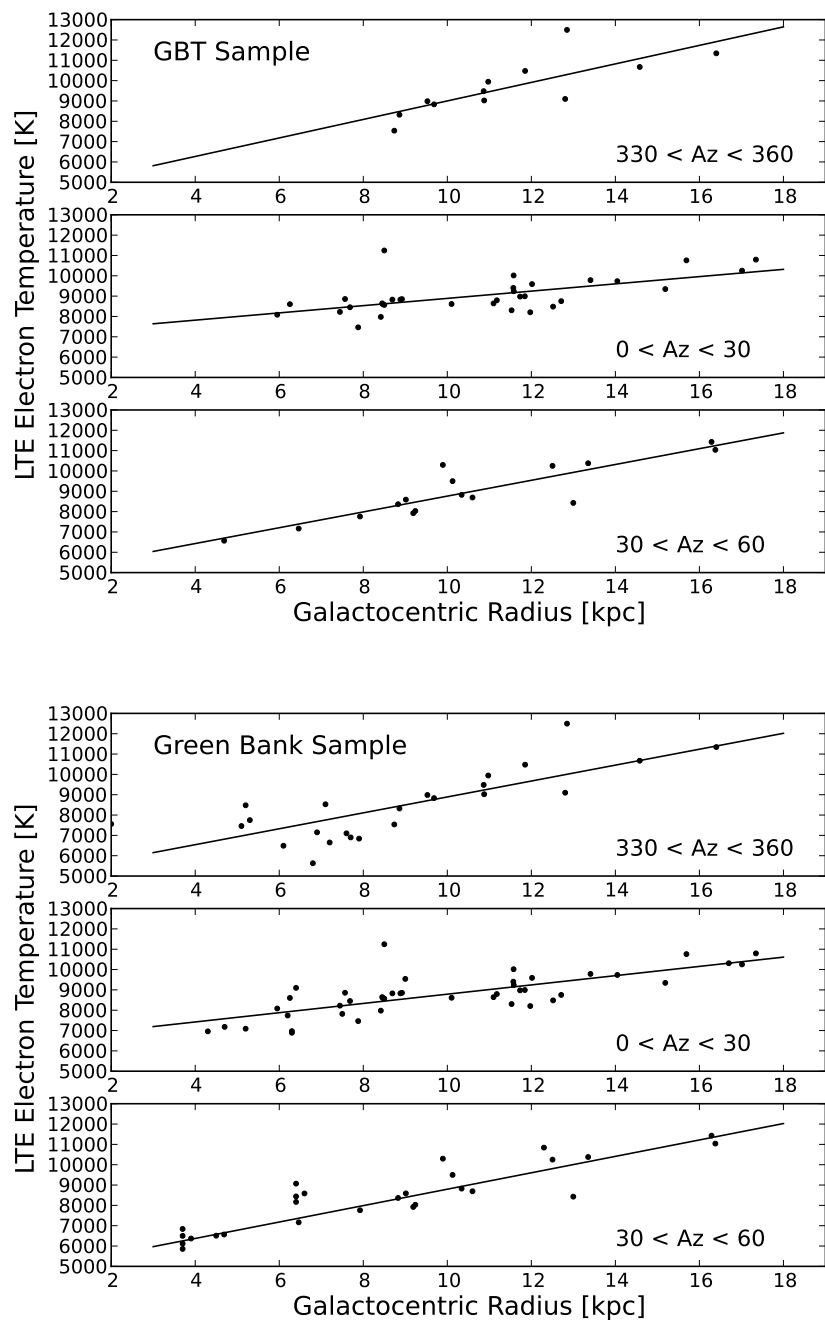


Fig. 6.— Electron temperature radial gradients for the GBT Sample (top) and the Green Bank Sample (bottom). Only quality factor values of C and better for both line and continuum data are included. The solid lines are linear least-squares fits to the data. Top panel:  $330^\circ < Az < 360^\circ$ . Middle panel:  $0^\circ < Az < 30^\circ$ . Bottom panel:  $30^\circ < Az < 60^\circ$ .

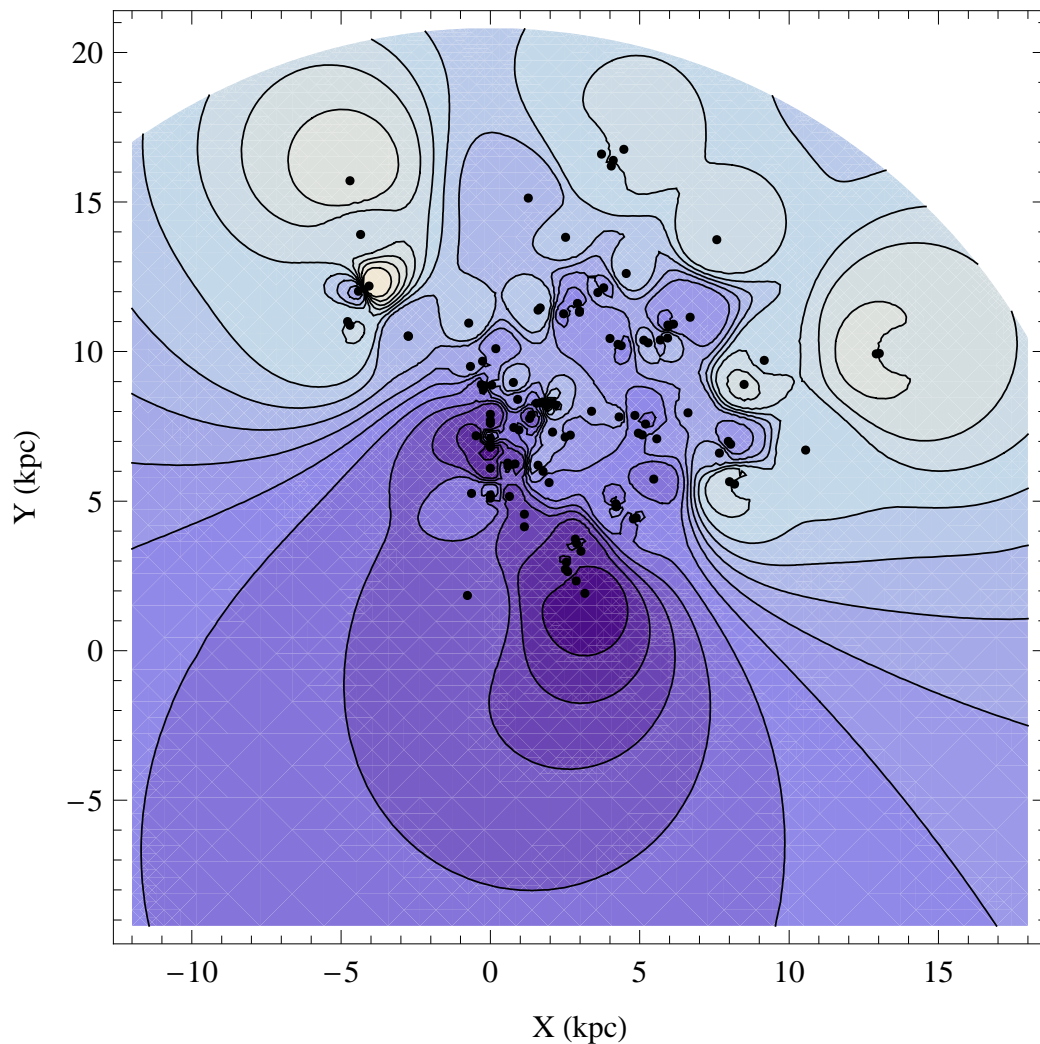


Fig. 7.— Image of the Galactic distribution of nebular electron temperatures produced from the discrete H II regions located between Galactic azimuth  $330^\circ$  and  $60^\circ$  for the Green Bank Sample (110 sources). The image was generated by using Shepard’s method with  $\alpha = 5$  (see text). The contours range between 6400 and 11200 K at intervals of 400 K. The darker shades are lower temperatures. The orientation is the same as in Figure 1 with the Galactic Center located at  $(x = 0, y = 0)$  and the Sun at 8.5 kpc above the Galactic Center at zero azimuth. The points indicate the location of the discrete H II regions.

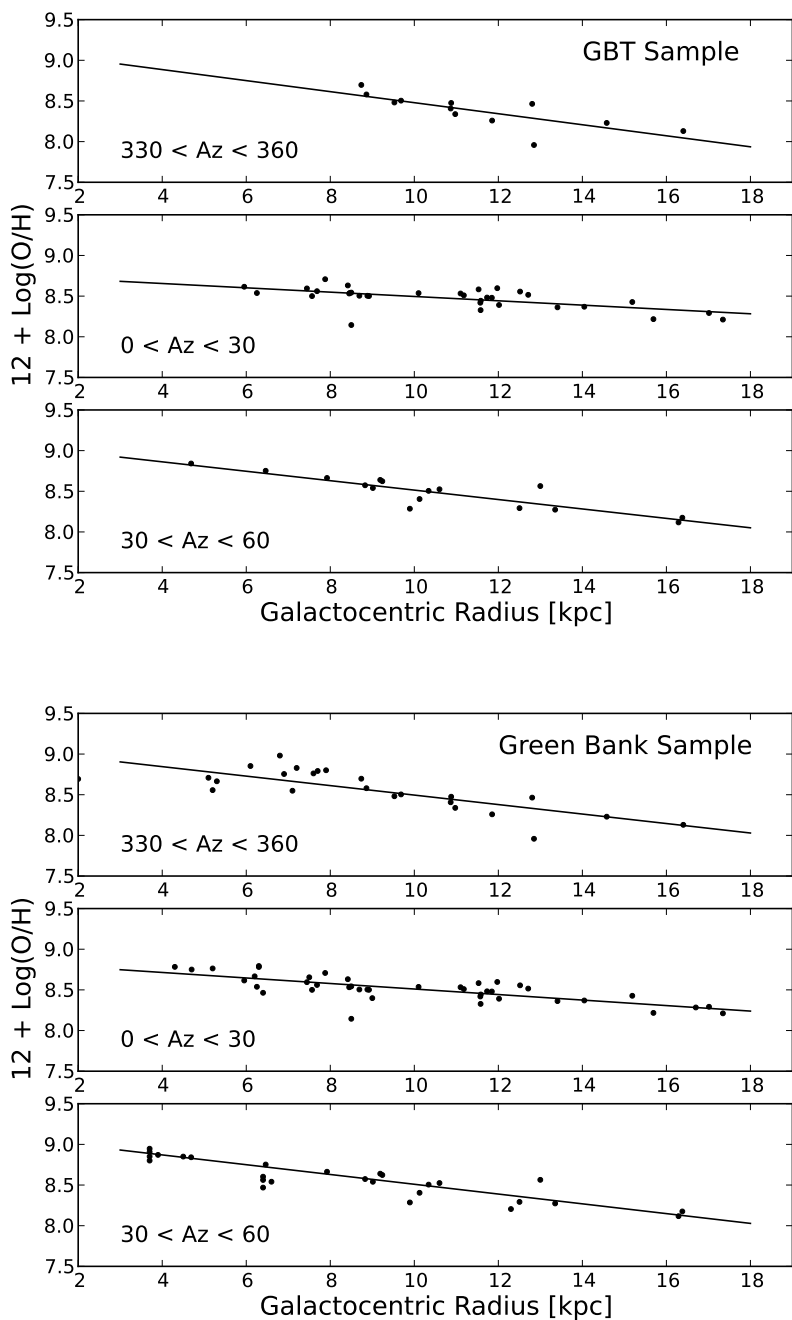


Fig. 8.— O/H abundance ratio radial gradient for the GBT Sample (top) and the Green Bank Sample (bottom). Only quality factor values of C and better for both line and continuum data are included. The solid lines are linear least-squares fits to the data. Top panel:  $330^\circ < Az < 360^\circ$ . Middle panel:  $0^\circ < Az < 30^\circ$ . Bottom panel:  $30^\circ < Az < 60^\circ$ .

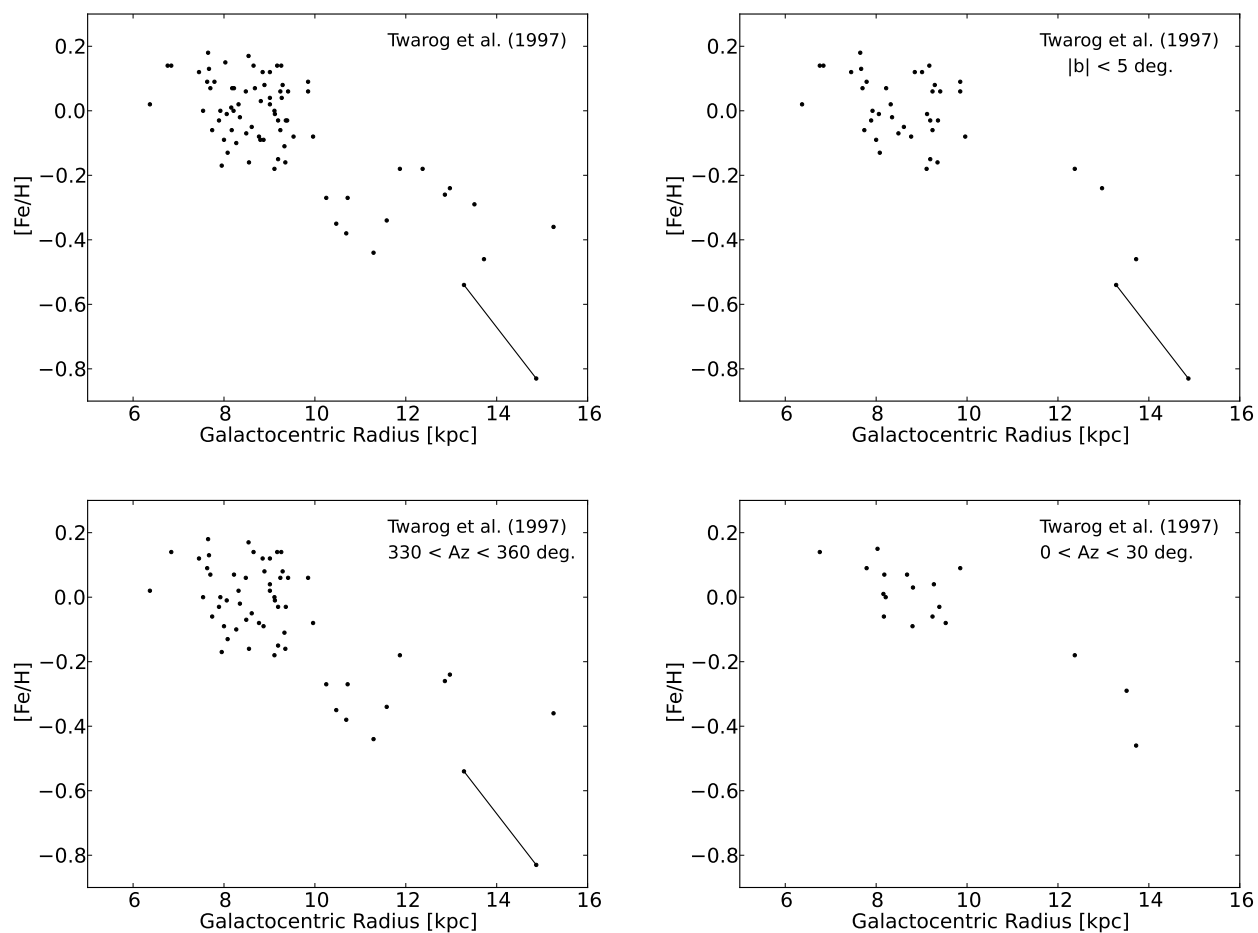


Fig. 9.—  $[\text{Fe}/\text{H}]$  abundance plotted as a function of Galactocentric radius from the open cluster data of Twarog et al. (1997). Top left panel: all data in their sample (cf. Figure 3 of Twarog et al.). Top right panel: only data within  $5^\circ$  of the Galactic plane are included. Bottom left panel: only data within the Galactic azimuth range  $330 - 360^\circ$ . Bottom right panel: only data within the Galactic azimuth range  $0 - 30^\circ$ . The solid line connects the two results for open cluster BE21.



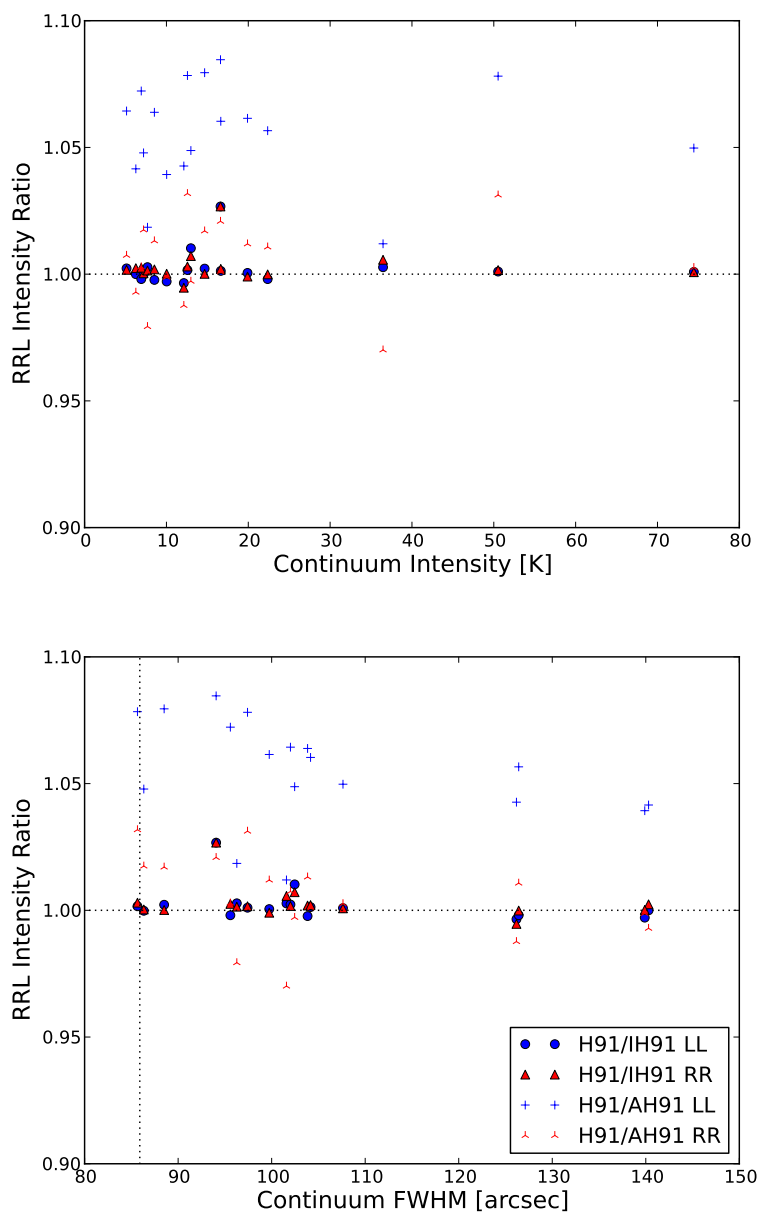


Fig. 10.— RRL intensity ratios as a function of continuum intensity (top) and FWHM angular size (bottom). Three different H91 $\alpha$  intensities have been calculated for all sources with a continuum intensity above 5 K: H91 is the H91 $\alpha$  intensity; IH91 is the H91 $\alpha$  intensity measured after the velocity scale has been interpolated; and AH91 is the H91 $\alpha$  intensity after the six adjacent RRLs have been interpolated and averaged. Plotted are the ratios: H91/IH91 and H91/AH91 for each polarization. The horizontal dashed line is a ratio of unity, whereas the vertical dashed line is the GBT’s HPBW. The H91/AH91 ratios are typically less than 5% and are not correlated with either continuum intensity or angular size.

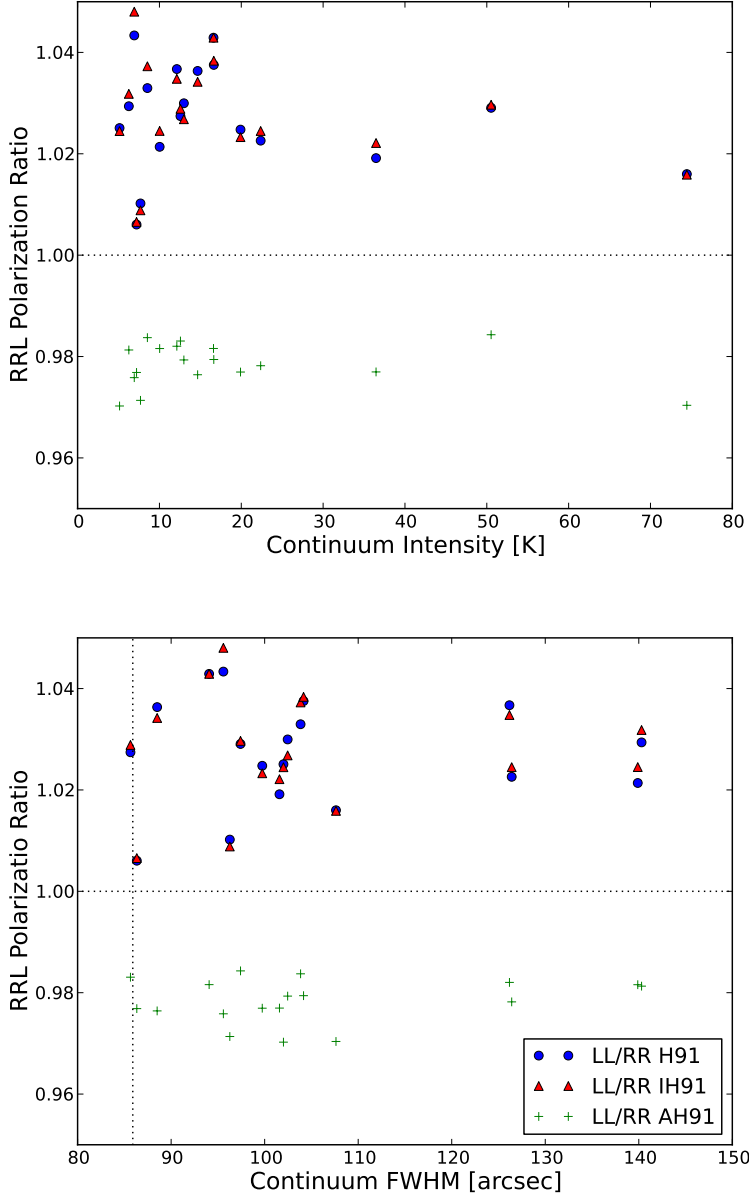


Fig. 11.— RRL polarization ratios as a function of continuum intensity (top) and FWHM angular size (bottom). Three different H91 $\alpha$  intensities have been calculated for all sources with a continuum intensity above 5 K: H91 is the H91 $\alpha$  intensity; IH91 is the H91 $\alpha$  intensity measured after the velocity scale has been interpolated; and AH91 is the H91 $\alpha$  intensity after the six adjacent RRLs have been interpolated and averaged. Plotted are the polarization ratios (LL/RR) for the H91, IH91, and AH91 RRL intensities. The horizontal dashed line is a ratio of unity, whereas the vertical dashed line is the GBT’s HPBW. The AH91 polarization ratios are typically less than 2% and are consistent with random errors in  $T_{\text{cal}}$ .

Table 1. Properties of Galactic H II Regions

Name	$\ell$ (deg)	$b$ (deg)	R.A. (B1950)	Decl. (B1950)	Az. (deg)	$R_{\text{gal}}$ (kpc)	$d_{\text{Sun}}$ (kpc)	$y$	$T_e$ (K)
G7.47+0.1	7.472	0.060	17 59 11.6	−22 27 55.0	169.635	21.9	30.3	0.083 ± 0.007	9929 ± 87
S64	28.788	3.491	18 28 50.4	−02 07 27.4	123.218	8.7	15.2	0.059 ± 0.006	8399 ± 73
W43	30.782	−0.028	18 45 00.9	−01 58 56.2	37.331	4.7	5.6	0.071 ± 0.004	6567 ± 30
G32.797+0.19	32.960	0.276	18 47 56.8	+00 05 31.0	109.783	7.6	13.2	0.078 ± 0.003	8625 ± 49
NRAO584	34.254	0.144	18 50 47.8	+01 10 46.0	19.242	6.0	3.5	0.053 ± 0.004	8084 ± 55
W48	35.196	−1.746	18 59 14.7	+01 08 42.4	16.382	6.3	3.1	0.072 ± 0.002	8603 ± 40
G38.875+0.308	38.875	0.308	18 58 44.8	+05 21 24.1	107.844	9.7	14.7	0.080 ± 0.000	8959 ± 232
G39.728-0.396	39.728	−0.396	19 02 50.5	+05 47 13.4	76.086	6.0	9.2	0.080 ± 0.000	8503 ± 255
S76	40.502	2.540	18 53 47.2	+07 49 40.6	7.369	7.4	1.5	0.045 ± 0.004	8223 ± 55
K47	45.454	0.059	19 12 00.1	+11 03 56.3	61.592	6.3	7.8	0.076 ± 0.003	8026 ± 63
G46.495-0.25	46.499	−0.251	19 15 07.3	+11 50 32.0	33.510	6.3	4.8	0.077 ± 0.006	5229 ± 40
W51	49.490	−0.381	19 21 24.9	+14 24 52.8	40.497	6.5	5.5	0.084 ± 0.001	7166 ± 25
G52.75+0.3	52.757	0.334	19 25 18.9	+17 37 32.0	70.451	8.1	9.6	0.065 ± 0.014	8970 ± 186
G55.11+2.4	55.114	2.422	19 22 19.8	+20 41 36.0	97.723	15.3	18.4	0.087 ± 0.009	13126 ± 144
G59.80+0.2	59.796	0.237	19 40 26.6	+23 42 44.0	63.685	8.8	9.1	0.057 ± 0.009	9068 ± 120
S87	60.883	−0.133	19 44 14.5	+24 27 54.0	9.607	7.9	1.5	0.080 ± 0.000	7463 ± 77
S88	61.477	0.094	19 44 42.4	+25 05 30.0	19.329	7.6	2.9	0.050 ± 0.002	8857 ± 43
S90	63.171	0.448	19 47 11.4	+26 43 46.6	43.621	7.9	6.1	0.076 ± 0.006	7760 ± 90
S93	64.136	−0.469	19 52 56.9	+27 05 00.0	20.353	7.7	3.0	0.050 ± 0.005	8452 ± 58
S98	68.144	0.918	19 57 10.5	+31 13 19.0	73.879	12.8	13.3	0.065 ± 0.013	10834 ± 207
G69.94+1.5	69.922	1.516	19 59 14.0	+33 02 49.0	71.327	12.8	12.9	0.085 ± 0.004	9703 ± 50
K3-50	70.292	1.598	19 59 50.5	+33 24 13.2	55.730	9.9	8.7	0.041 ± 0.007	10297 ± 121
G75.77+0.3	75.767	0.344	20 19 49.0	+37 16 18.0	38.157	9.0	5.7	0.076 ± 0.003	8590 ± 47
G75.834+0.40	75.834	0.402	20 19 46.3	+37 21 35.0	35.173	8.8	5.2	0.077 ± 0.002	8363 ± 32
G76.15-0.3	76.152	−0.281	20 23 29.9	+37 13 30.0	49.250	10.1	7.9	0.061 ± 0.010	9498 ± 119
S106	76.383	−0.623	20 25 34.2	+37 12 46.0	13.513	8.5	2.0	0.028 ± 0.006	11245 ± 92
G77.98+0.0	77.972	−0.012	20 27 48.7	+38 51 27.0	30.788	8.8	4.6	0.072 ± 0.012	7674 ± 111
G78.03+0.6	78.032	0.607	20 25 25.0	+39 16 11.0	11.919	8.5	1.8	0.061 ± 0.008	8567 ± 86
S108	78.142	1.814	20 20 38.4	+40 03 36.0	11.803	8.5	1.7	0.068 ± 0.008	8596 ± 107
DR7	79.293	1.303	20 26 20.0	+40 41 57.0	48.709	10.6	8.1	0.079 ± 0.006	8693 ± 86
G79.42+2.4	79.417	2.414	20 21 55.7	+41 26 48.0	10.567	8.4	1.6	0.080 ± 0.000	7977 ± 222
G79.96+0.9	79.957	0.866	20 30 16.5	+40 58 31.0	34.420	9.2	5.3	0.080 ± 0.000	7921 ± 294
G80.35+0.7	80.352	0.724	20 32 08.0	+41 12 26.0	57.567	12.5	10.7	0.057 ± 0.011	10250 ± 155
G80.88+0.4	80.880	0.410	20 35 09.9	+41 26 16.0	9.076	8.5	1.3	0.089 ± 0.010	9032 ± 109
G80.94-0.1	80.938	−0.130	20 37 37.8	+41 09 16.0	28.857	8.9	4.4	0.042 ± 0.005	8853 ± 62
G81.25+1.1	81.253	1.123	20 33 19.9	+42 09 59.0	8.763	8.4	1.3	0.047 ± 0.008	8065 ± 101
DR21	81.681	0.540	20 37 14.0	+42 09 06.0	22.947	8.7	3.4	0.063 ± 0.003	8829 ± 36
G82.57+0.4	82.582	0.411	20 40 47.7	+42 46 55.0	31.587	9.2	4.9	0.064 ± 0.011	8030 ± 128
S112	83.781	3.315	20 32 02.1	+45 30 09.0	6.214	8.4	0.9	0.093 ± 0.016	8643 ± 184
G85.24+0.0	85.246	0.014	20 51 49.6	+44 35 33.0	39.751	10.3	6.6	0.081 ± 0.015	8824 ± 177
S127A	96.291	2.596	21 27 06.0	+54 24 06.0	52.465	16.3	13.0	0.060 ± 0.018	11428 ± 305
WB85A	96.297	2.597	21 27 07.6	+54 24 22.0	52.651	16.4	13.1	0.135 ± 0.027	11039 ± 314
S128	97.516	3.172	21 30 36.9	+55 39 25.0	43.350	13.4	9.2	0.130 ± 0.024	10378 ± 251
S146	108.196	0.577	22 47 30.4	+59 38 52.0	29.584	12.0	6.2	0.079 ± 0.004	9590 ± 59
S147	108.368	−1.057	22 54 15.3	+58 15 12.0	28.707	11.8	6.0	0.080 ± 0.000	8992 ± 131

Table 1—Continued

Name	$\ell$ (deg)	$b$ (deg)	R.A. (B1950)	Decl. (B1950)	Az. (deg)	$R_{\text{gal}}$ (kpc)	$d_{\text{Sun}}$ (kpc)	$y$	$T_{\text{e}}$ (K)
S152	108.759	-0.951	22 56 37.1	+58 30 54.0	27.169	11.6	5.6	$0.034 \pm 0.006$	$9404 \pm 81$
S156	110.106	0.044	23 03 04.3	+59 58 20.0	26.328	11.6	5.5	$0.067 \pm 0.007$	$9240 \pm 75$
NGC7538	111.525	0.816	23 11 21.8	+61 13 38.0	29.300	12.5	6.6	$0.082 \pm 0.003$	$8483 \pm 51$
S159	111.612	0.374	23 13 21.3	+60 50 49.0	30.947	13.0	7.2	$0.031 \pm 0.006$	$8428 \pm 68$
S162	112.223	0.227	23 18 29.2	+60 55 24.0	22.635	11.1	4.6	$0.063 \pm 0.009$	$8641 \pm 118$
S168	115.789	-1.579	23 50 30.0	+60 12 04.0	21.004	11.2	4.5	$0.080 \pm 0.000$	$8794 \pm 242$
WB380	124.644	2.539	01 04 36.3	+65 05 22.0	28.891	15.7	9.2	$0.080 \pm 0.000$	$10758 \pm 288$
S186	124.897	0.321	01 05 38.8	+62 51 35.3	17.133	11.3	4.1	$0.080 \pm 0.000$	$8975 \pm 460$
WB399B	128.777	2.012	01 42 05.7	+64 01 00.0	29.695	18.1	11.5	$0.080 \pm 0.000$	$10361 \pm 427$
G132.16-0.7	132.157	-0.725	02 04 29.1	+60 31 46.0	19.811	13.4	6.1	$0.076 \pm 0.010$	$9785 \pm 123$
W3	133.720	1.223	02 21 56.9	+61 52 40.0	14.703	11.7	4.1	$0.082 \pm 0.002$	$8977 \pm 38$
G133.790+1.4	133.785	1.423	02 23 04.0	+62 02 32.1	17.348	12.7	5.2	$0.088 \pm 0.006$	$8752 \pm 74$
G136.91+1.0	136.900	1.060	02 45 41.8	+60 28 46.0	14.085	12.0	4.3	$0.080 \pm 0.000$	$8204 \pm 257$
S201	138.494	1.641	02 59 18.9	+60 16 15.0	12.261	11.5	3.7	$0.080 \pm 0.000$	$8302 \pm 131$
S206	150.593	-0.951	03 59 29.8	+51 10 38.0	8.278	11.6	3.4	$0.075 \pm 0.005$	$10016 \pm 83$
S209	151.606	-0.240	04 07 19.7	+51 01 58.0	14.918	17.3	9.4	$0.070 \pm 0.006$	$10795 \pm 98$
S211	154.649	2.438	04 32 59.6	+50 46 31.0	10.334	14.0	5.9	$0.080 \pm 0.000$	$9734 \pm 175$
S212	155.357	2.609	04 36 46.8	+50 21 58.0	12.620	17.0	8.9	$0.088 \pm 0.024$	$10253 \pm 309$
S228	169.191	-0.903	05 10 01.8	+37 23 32.0	4.785	15.2	6.8	$0.080 \pm 0.000$	$9345 \pm 179$
S235	173.599	2.798	05 37 37.8	+35 49 35.0	1.019	10.1	1.6	$0.080 \pm 0.000$	$8612 \pm 137$
S237	173.899	0.288	05 28 08.1	+34 12 39.0	0.264	8.9	0.4	$0.080 \pm 0.000$	$8829 \pm 158$
S257	192.626	-0.017	06 10 08.7	+17 59 46.0	358.435	9.7	1.2	$0.080 \pm 0.000$	$8833 \pm 107$
S269	196.456	-1.670	06 11 48.8	+13 50 40.0	356.218	11.0	2.6	$0.080 \pm 0.000$	$9945 \pm 164$
G201.6+1.6	201.682	1.652	06 33 53.8	+10 48 10.5	353.204	12.2	3.9	$0.080 \pm 0.000$	$10063 \pm 283$
OriA	209.011	-19.384	05 32 49.0	-05 25 16.0	358.714	8.9	0.4	$0.082 \pm 0.001$	$8322 \pm 55$
WB870	213.077	-2.215	06 41 16.4	-01 05 14.0	343.352	16.4	8.6	$0.080 \pm 0.000$	$11343 \pm 162$
MONR2	213.704	-12.606	06 05 19.5	-06 22 38.2	355.975	9.5	1.2	$0.017 \pm 0.005$	$8986 \pm 65$
S288	218.739	1.848	07 06 09.9	-04 14 14.0	342.672	14.6	6.9	$0.045 \pm 0.009$	$14578 \pm 195$
WB952	218.740	1.848	07 06 10.0	-04 14 17.0	342.657	14.6	6.9	$0.080 \pm 0.000$	$10671 \pm 143$
S291	220.521	-2.767	06 53 00.3	-07 56 56.2	337.916	17.5	10.1	$0.080 \pm 0.000$	$12037 \pm 725$
S297	225.472	-2.578	07 02 55.7	-12 15 12.0	358.434	8.7	0.3	$0.080 \pm 0.000$	$7537 \pm 158$
S298	227.796	-0.135	07 16 14.0	-13 10 07.1	341.548	12.8	5.5	$0.111 \pm 0.014$	$12495 \pm 249$
RCW6	231.491	-4.384	07 07 46.8	-18 25 00.7	339.802	12.8	5.7	$0.080 \pm 0.000$	$9098 \pm 286$
RCW8	233.760	-0.203	07 27 50.0	-18 26 24.0	345.360	10.9	3.4	$0.080 \pm 0.000$	$9482 \pm 209$
S305	233.761	-0.191	07 27 52.8	-18 26 08.0	345.310	10.9	3.4	$0.080 \pm 0.000$	$9024 \pm 206$
S311	243.166	0.364	07 50 17.6	-26 18 28.2	336.623	11.9	5.3	$0.079 \pm 0.012$	$10477 \pm 214$

Table 2. Radio Recombination Line Parameters of Galactic H II Regions

Name	Atom	$T_L$ (mK)	$\sigma T_L$ (mK)	$\Delta V$ (km s <sup>-1</sup> )	$\sigma \Delta V$ (km s <sup>-1</sup> )	$V_{LSR}$ (km s <sup>-1</sup> )	$\sigma V_{LSR}$ (km s <sup>-1</sup> )	$t_{intg}$ (hr)	rms (mK)	QF
G7.47+0.1	H	192.51	0.90	32.98	0.18	-16.93	0.08	4.8	5.49	B
	He	21.05	1.05	25.18	1.62	-17.34	0.63	...	...	...
	C	14.29	1.84	8.06	1.26	-15.78	0.52	...	...	...
S64	H	391.96	1.82	21.00	0.11	-1.07	0.05	2.4	7.97	B
	He	36.70	2.30	13.12	0.95	-1.52	0.40	...	...	...
	C	58.68	5.13	2.63	0.27	8.88	0.11	...	...	...
W43	H	2032.18	3.68	33.51	0.07	89.84	0.03	2.4	12.11	A
	He	158.98	4.04	30.47	1.31	88.98	0.51	...	...	...
G32.797+0.19	H	539.84	1.34	29.49	0.08	14.90	0.04	4.8	5.85	A
	He	52.52	1.51	23.76	0.81	15.33	0.33	...	...	...
	C	26.70	2.68	7.58	0.93	12.99	0.38	...	...	...
NRAO584	H	1661.73	4.86	24.42	0.08	53.11	0.04	2.4	10.99	A
	He	132.50	6.00	16.18	0.86	52.62	0.36	...	...	...
	C	40.11	9.04	7.07	1.88	57.36	0.79	...	...	...
W48	H	1885.31	2.53	23.55	0.04	46.00	0.02	2.4	11.00	A
	He	201.76	3.09	15.81	0.28	46.23	0.12	...	...	...
	C	84.68	5.22	5.53	0.39	41.96	0.17	...	...	...
G38.875+0.308	H	48.24	0.90	28.79	0.63	-14.98	0.26	2.4	6.11	C
G39.728-0.396	H	46.92	1.01	25.67	0.67	57.68	0.27	2.4	5.78	C
S76	H	355.60	1.18	22.44	0.09	21.74	0.04	2.4	6.68	A
	He	25.12	1.49	14.34	1.04	19.84	0.42	...	...	...
	C	35.86	3.43	2.69	0.30	32.86	0.13	...	...	...
K47	H	742.94	1.64	27.62	0.07	54.21	0.03	2.4	7.95	A
	He	76.45	1.98	20.40	0.74	54.08	0.28	...	...	...
G46.495-0.25	H	257.77	1.10	18.32	0.09	57.68	0.04	4.4	4.91	A
	He	26.45	1.27	13.81	0.78	57.53	0.32	...	...	...
W51	H	6720.34	5.88	30.16	0.03	55.95	0.01	2.4	28.10	A
	He	663.06	6.60	25.52	0.35	56.00	0.13	...	...	...
	C	110.95	10.31	10.28	1.23	57.17	0.50	...	...	...
G52.75+0.3	H	59.22	0.74	25.45	0.37	11.18	0.16	4.8	4.18	C
	He	6.81	0.98	14.29	2.40	9.99	1.01	...	...	...
G55.11+2.4	H	49.39	0.29	32.01	0.22	-76.22	0.09	23.9	1.75	B
	He	4.16	0.29	33.16	2.72	-78.01	1.12	...	...	...
G59.80+0.2	H	106.76	0.82	21.83	0.19	-3.73	0.08	4.4	4.52	B
	He	9.55	1.03	13.97	1.73	-4.05	0.74	...	...	...
S87	H	114.01	0.86	21.21	0.18	17.53	0.08	5.0	4.65	B
	C	38.96	1.90	4.34	0.25	20.85	0.10	...	...	...
S88	H	810.84	1.61	26.03	0.06	26.03	0.03	2.4	7.96	A
	He	61.00	1.98	17.34	0.65	28.28	0.28	...	...	...
	C	106.08	3.61	5.20	0.20	20.41	0.09	...	...	...
S90	H	197.08	0.92	25.15	0.14	16.77	0.06	4.8	4.46	B
	He	18.23	1.01	20.70	1.32	16.45	0.56	...	...	...
S93	H	218.61	0.84	23.87	0.11	23.32	0.05	4.8	4.49	B
	He	17.41	1.06	15.13	1.06	23.56	0.45	...	...	...
	C	13.61	1.60	6.61	0.91	20.66	0.38	...	...	...

Table 2—Continued

Name	Atom	$T_L$ (mK)	$\sigma T_L$ (mK)	$\Delta V$ (km s <sup>-1</sup> )	$\sigma \Delta V$ (km s <sup>-1</sup> )	$V_{LSR}$ (km s <sup>-1</sup> )	$\sigma V_{LSR}$ (km s <sup>-1</sup> )	$t_{\text{intg}}$ (hr)	rms (mK)	QF
S98	H	47.82	0.54	24.70	0.32	-64.69	0.14	9.5	2.98	C
	He	5.51	0.71	13.92	2.09	-63.94	0.88	...	...	...
G69.94+1.5	H	364.80	0.90	26.98	0.08	-64.77	0.03	4.8	4.93	A
	He	39.56	1.05	21.03	0.75	-65.60	0.29	...	...	...
K3-50	H	656.17	3.49	36.96	0.23	-25.57	0.10	2.4	9.97	A
	He	41.67	4.42	23.91	3.17	-24.69	1.26	...	...	...
	C	58.19	6.42	10.93	1.48	-26.33	0.62	...	...	...
G75.77+0.3	H	547.20	1.11	28.17	0.07	-8.81	0.03	4.0	5.93	A
	He	56.16	1.33	20.73	0.63	-9.61	0.25	...	...	...
	C	18.81	2.71	4.91	0.85	-2.10	0.35	...	...	...
G75.834+0.40	H	1101.76	1.46	30.53	0.05	-4.68	0.02	2.4	8.75	A
	He	97.48	1.60	26.50	0.58	-5.81	0.22	...	...	...
	C	46.21	4.00	4.31	0.45	0.34	0.18	...	...	...
G76.15-0.3	H	117.59	0.79	30.88	0.24	-30.48	0.10	4.8	5.10	B
	He	8.54	0.88	25.74	3.22	-31.36	1.30	...	...	...
	C	10.23	1.95	5.12	1.15	-30.23	0.48	...	...	...
S106	H	675.66	3.22	42.02	0.23	3.04	0.10	2.4	14.43	B
	He	29.79	4.10	26.50	4.37	2.70	1.79	...	...	...
	C	45.02	6.20	11.36	1.86	-4.30	0.78	...	...	...
G77.98+0.0	H	169.85	1.22	28.69	0.24	-3.59	0.10	2.4	7.01	B
	He	10.93	1.16	31.92	3.92	-7.64	1.66	...	...	...
G78.03+0.6	H	213.28	1.22	27.24	0.18	1.25	0.08	2.4	6.82	B
	He	17.39	1.41	20.22	1.89	1.93	0.80	...	...	...
S108	H	180.08	1.23	24.60	0.19	3.88	0.08	2.4	7.23	B
	He	19.73	1.55	15.37	1.39	6.56	0.59	...	...	...
DR7	H	456.47	1.81	30.01	0.14	-38.83	0.06	4.8	5.56	A
	He	50.09	2.16	21.73	1.17	-37.82	0.47	...	...	...
	C	14.91	2.92	12.43	3.69	-39.60	1.33	...	...	...
G79.42+2.4	H	49.85	0.86	20.79	0.55	5.17	0.18	4.8	4.46	C
G79.96+0.9	H	39.27	1.05	23.01	0.73	-12.76	0.30	4.8	5.09	C
G80.35+0.7	H	107.68	0.93	26.46	0.26	-65.13	0.11	4.8	5.46	C
	He	9.74	1.17	16.75	2.33	-65.55	0.98	...	...	...
G80.88+0.4	H	133.09	0.90	23.18	0.18	0.24	0.08	4.8	4.99	B
	He	13.82	0.98	19.76	1.62	0.20	0.68	...	...	...
G80.94-0.1	H	595.13	1.82	28.66	0.10	-6.89	0.04	2.4	7.20	A
	He	27.25	1.96	26.33	2.59	-8.79	0.99	...	...	...
	C	28.37	4.44	5.24	1.00	-2.89	0.39	...	...	...
G81.25+1.1	H	122.62	0.93	22.90	0.20	10.60	0.09	4.8	4.94	B
	He	11.15	1.30	11.82	1.59	9.78	0.68	...	...	...
DR21	H	2215.95	3.86	35.91	0.07	-1.57	0.03	2.4	16.54	A
	He	162.67	4.30	31.02	1.16	-2.20	0.44	...	...	...
	C	56.04	7.79	14.99	2.15	-8.12	1.09	...	...	...
G82.57+0.4	H	165.36	1.55	23.43	0.25	-13.91	0.11	2.4	8.17	B
	He	18.53	2.05	13.31	1.70	-15.47	0.72	...	...	...
S112	H	66.11	0.84	23.08	0.34	5.56	0.14	4.8	4.52	C

Table 2—Continued

Name	Atom	$T_L$ (mK)	$\sigma T_L$ (mK)	$\Delta V$ (km s <sup>-1</sup> )	$\sigma \Delta V$ (km s <sup>-1</sup> )	$V_{LSR}$ (km s <sup>-1</sup> )	$\sigma V_{LSR}$ (km s <sup>-1</sup> )	$t_{\text{intg}}$ (hr)	rms (mK)	QF
G85.24+0.0	He	9.13	1.02	15.56	2.00	5.61	0.85	...	...	...
	H	84.41	0.89	26.88	0.33	-35.09	0.14	4.8	5.23	C
S127A	He	7.48	0.92	24.65	3.52	-33.80	1.49	...	...	...
	H	41.61	0.67	28.72	0.54	-99.92	0.22	4.8	4.20	C
WB85A	He	4.53	0.89	15.76	3.59	-98.57	1.52	...	...	...
	H	39.99	0.56	27.74	0.45	-100.57	0.19	7.2	3.33	C
S128	He	4.00	0.49	37.45	5.98	-107.36	2.33	...	...	...
	H	61.66	0.70	26.99	0.36	-74.72	0.15	4.8	4.20	C
S146	He	5.14	0.57	42.20	6.11	-82.96	2.38	...	...	...
	H	262.53	0.77	25.77	0.09	-57.07	0.04	4.8	4.29	A
S147	He	29.43	0.94	18.05	0.76	-58.03	0.29	...	...	...
	C	9.28	1.50	6.90	1.38	-49.75	0.57	...	...	...
	H	65.22	0.69	26.10	0.32	-54.88	0.14	4.8	3.92	C
S152	C	12.92	1.52	5.43	0.74	-54.18	0.31	...	...	...
	H	147.49	0.69	29.57	0.16	-51.28	0.07	4.8	4.08	B
S156	He	7.38	0.83	20.23	2.67	-52.95	1.12	...	...	...
	C	23.69	1.86	4.04	0.37	-50.77	0.16	...	...	...
	H	190.93	0.74	38.05	0.17	-50.96	0.07	4.8	4.52	B
NGC7538	He	12.47	0.75	38.91	3.46	-53.92	1.35	...	...	...
	C	22.07	2.26	4.49	0.57	-50.69	0.21	...	...	...
	H	1005.76	1.87	27.07	0.06	-61.60	0.02	2.4	9.37	A
S159	He	106.75	2.19	20.92	0.56	-62.37	0.22	...	...	...
	C	13.05	3.61	7.52	2.57	-56.75	1.06	...	...	...
	H	177.33	0.84	26.82	0.15	-66.68	0.06	4.8	4.75	B
S162	He	10.77	1.20	13.75	1.92	-70.46	0.76	...	...	...
	C	31.13	2.14	4.22	0.35	-57.67	0.15	...	...	...
	H	102.00	0.73	28.81	0.24	-43.86	0.10	4.8	4.34	B
S168	He	9.80	0.90	18.96	2.02	-47.93	0.85	...	...	...
	H	40.18	0.78	26.79	0.63	-43.67	0.25	4.8	4.28	C
WB380	H	32.67	0.62	29.73	0.70	-79.13	0.28	4.4	4.05	C
S186	H	19.48	0.73	26.98	1.19	-41.63	0.50	4.8	4.25	D
WB399B	H	7.84	0.23	20.92	0.71	-87.20	0.30	49.0	1.18	D
	C	7.71	0.63	2.73	0.26	-83.07	0.11	...	...	...
G132.16-0.7	H	79.61	0.54	24.93	0.20	-56.39	0.08	9.5	3.09	B
	He	6.76	0.58	22.37	2.21	-54.41	0.93	...	...	...
	C	8.36	1.26	4.68	0.82	-56.49	0.35	...	...	...
W3	H	3837.85	4.75	27.69	0.04	-40.68	0.02	18.7	13.58	A
	He	401.81	5.40	21.76	0.34	-40.83	0.14	...	...	...
	C	183.21	10.60	6.01	0.50	-40.13	0.19	...	...	...
G133.790+1.4	H	787.00	2.97	27.46	0.12	-49.42	0.05	4.8	5.56	A
	He	87.03	3.46	21.75	1.25	-50.87	0.48	...	...	...
G136.91+1.0	H	26.84	0.58	23.49	0.60	-40.65	0.25	9.5	2.92	C
S201	H	79.63	0.78	23.80	0.27	-35.47	0.11	4.8	3.89	B
	C	19.95	2.03	3.47	0.41	-39.72	0.17	...	...	...
S206	H	219.24	0.80	27.83	0.12	-26.61	0.05	4.8	4.93	B

Table 2—Continued

Name	Atom	$T_L$ (mK)	$\sigma T_L$ (mK)	$\Delta V$ (km s <sup>-1</sup> )	$\sigma \Delta V$ (km s <sup>-1</sup> )	$V_{LSR}$ (km s <sup>-1</sup> )	$\sigma V_{LSR}$ (km s <sup>-1</sup> )	$t_{intg}$ (hr)	rms (mK)	QF
S209	He	22.43	0.93	20.52	0.99	-26.98	0.42	...	...	...
	H	160.45	0.71	31.66	0.16	-51.18	0.07	9.5	3.28	B
	He	13.10	0.77	27.34	1.91	-52.55	0.79	...	...	...
S211	C	12.10	2.00	4.13	0.83	-55.01	0.34	...	...	...
	H	50.04	0.66	28.55	0.44	-35.22	0.18	4.8	3.99	C
S212	C	6.93	1.46	5.78	1.41	-41.17	0.60	...	...	...
	H	45.43	0.76	25.57	0.50	-43.95	0.21	4.8	4.32	C
S228	He	4.61	0.82	22.16	4.55	-46.70	1.93	...	...	...
	H	60.90	0.82	23.09	0.36	-17.31	0.15	4.8	4.28	C
S235	C	19.31	2.37	2.75	0.39	-6.44	0.17	...	...	...
	H	81.78	0.94	20.86	0.28	-25.61	0.12	4.8	4.54	C
S237	H	62.54	0.76	22.98	0.32	-0.64	0.14	4.8	4.10	C
	C	18.40	2.26	2.57	0.37	-9.34	0.15	...	...	...
S257	H	105.83	0.88	22.12	0.22	5.05	0.09	4.8	4.31	B
S269	H	61.61	0.74	24.23	0.34	12.87	0.14	4.8	4.11	C
	C	27.59	2.39	2.34	0.23	18.10	0.10	...	...	...
G201.6+1.6	H	25.59	0.51	25.91	0.63	23.14	0.25	9.5	3.34	C
OriA	H	9728.44	6.99	26.13	0.02	-2.25	0.01	2.4	35.84	A
	He	1160.24	8.74	18.05	0.20	-2.31	0.07	...	...	...
	C	323.49	15.63	5.92	0.36	8.91	0.14	...	...	...
WB870	H	68.31	0.70	28.56	0.34	55.32	0.14	4.8	4.46	C
MONR2	H	942.25	3.54	29.81	0.13	10.82	0.05	2.4	8.51	A
	He	20.10	3.94	24.21	5.55	11.65	2.33	...	...	...
S288	C	144.47	8.44	5.38	0.38	9.08	0.15	...	...	...
	H	70.43	0.55	24.52	0.22	54.49	0.09	9.5	3.04	B
	He	5.85	0.76	13.14	1.96	54.53	0.83	...	...	...
WB952	C	9.80	1.33	4.24	0.67	56.05	0.28	...	...	...
	H	73.83	0.74	24.62	0.29	54.54	0.12	4.8	4.32	C
S291	H	5.40	0.23	31.82	1.69	70.33	0.67	39.6	1.60	D
S297	H	40.34	0.58	22.59	0.37	1.94	0.16	9.1	3.01	C
	C	23.10	1.98	1.90	0.19	12.26	0.08	...	...	...
S298	H	15.09	0.17	28.89	0.37	51.89	0.16	108.8	0.97	C
	He	2.31	0.19	20.90	2.04	52.12	0.86	...	...	...
RCW6	H	42.21	0.98	20.54	0.55	54.25	0.23	4.8	5.06	C
RCW8	H	54.33	0.83	24.06	0.43	35.31	0.18	4.8	4.54	C
S305	H	51.88	0.79	26.05	0.47	35.44	0.20	4.8	4.57	C
S311	H	98.12	0.94	22.29	0.25	51.68	0.10	4.8	5.19	C
	He	12.56	1.19	13.77	1.52	53.05	0.64	...	...	...



Table 3. Radio Continuum Parameters of Galactic H II Regions

Name	R.A.				Decl.				Average				QF
	$T_C$ (K)	$\sigma T_C$ (K)	$\Theta$ ( $\prime$ )	$\sigma \Theta$ ( $\prime$ )	$T_C$ (K)	$\sigma T_C$ (K)	$\Theta$ ( $\prime$ )	$\sigma \Theta$ ( $\prime$ )	$T_C$ (K)	$\sigma T_C$ (K)	$\Theta$ ( $\prime$ )	$\sigma \Theta$ ( $\prime$ )	
G7.47+0.1	3.370	0.015	1.472	0.008	3.417	0.019	1.446	0.009	3.393	0.012	1.459	0.006	A
S64	3.583	0.029	5.609	0.099	3.507	0.017	4.960	0.039	3.545	0.017	5.274	0.051	C
W43	22.099	0.071	2.462	0.016	22.639	0.118	1.803	0.024	22.369	0.069	2.107	0.015	C
G32.797+0.19	7.250	0.043	1.439	0.010	7.155	0.046	1.439	0.011	7.202	0.031	1.439	0.007	A
NRAO584	16.404	0.144	1.824	0.019	16.877	0.116	1.652	0.013	16.641	0.092	1.736	0.011	A
W48	20.117	0.123	1.642	0.012	19.696	0.142	1.683	0.014	19.907	0.094	1.662	0.009	A
G38.875+0.308	0.638	0.008	1.367	0.020	0.676	0.005	1.428	0.013	0.657	0.005	1.397	0.012	B
G39.728-0.396	0.542	0.006	1.530	0.020	0.532	0.004	1.458	0.014	0.537	0.004	1.493	0.012	B
S76	3.322	0.026	1.922	0.018	3.303	0.011	1.791	0.007	3.312	0.014	1.855	0.009	B
K47	7.901	0.075	1.730	0.019	9.154	0.109	1.732	0.024	8.528	0.066	1.731	0.016	C
G46.495-0.25	1.156	0.006	2.638	0.023	1.245	0.003	3.967	0.012	1.201	0.003	3.235	0.015	D
W51	74.962	0.309	1.756	0.011	73.925	0.458	1.833	0.014	74.443	0.276	1.794	0.009	B
G52.75+0.3	0.711	0.005	1.529	0.013	0.697	0.005	1.538	0.012	0.704	0.004	1.534	0.009	B
G55.11+2.4	1.168	0.004	1.521	0.007	1.169	0.003	1.547	0.004	1.169	0.003	1.534	0.004	A
G59.80+0.2	1.081	0.007	1.833	0.014	1.109	0.005	1.841	0.009	1.095	0.004	1.837	0.008	A
S87	0.900	0.004	1.564	0.008	0.955	0.005	1.462	0.009	0.928	0.003	1.512	0.006	B
S88	9.476	0.069	1.487	0.013	9.700	0.037	1.460	0.007	9.588	0.039	1.474	0.007	B
S90	1.993	0.026	2.895	0.044	1.971	0.028	2.922	0.048	1.982	0.019	2.908	0.032	B
S93	2.270	0.009	1.655	0.008	2.224	0.009	1.616	0.008	2.247	0.006	1.635	0.005	A
S98	0.687	0.005	1.954	0.017	0.685	0.007	1.830	0.022	0.686	0.004	1.891	0.014	B
G69.94+1.5	5.115	0.029	1.731	0.011	5.139	0.012	1.670	0.005	5.127	0.016	1.700	0.006	A
K3-50	13.066	0.022	1.520	0.003	12.907	0.219	1.918	0.042	12.987	0.110	1.708	0.019	B
G75.77+0.3	6.924	0.051	1.595	0.014	6.923	0.045	1.591	0.012	6.923	0.034	1.593	0.009	B
G75.834+0.40	14.587	0.053	1.479	0.006	14.745	0.085	1.471	0.011	14.666	0.050	1.475	0.006	B
G76.15-0.3	1.776	0.011	1.555	0.011	1.834	0.012	1.552	0.011	1.805	0.008	1.553	0.008	C
S106	16.875	0.049	1.473	0.005	16.338	0.028	1.668	0.003	16.606	0.028	1.568	0.003	B
G77.98+0.0	1.932	0.020	2.855	0.035	1.900	0.014	2.150	0.024	1.916	0.012	2.478	0.020	D
G78.03+0.6	2.568	0.009	3.375	0.018	2.562	0.012	3.557	0.026	2.565	0.007	3.465	0.015	B
S108	2.036	0.014	3.597	0.036	1.920	0.019	2.944	0.041	1.978	0.012	3.254	0.028	C
DR7	6.129	0.060	2.169	0.035	6.393	0.083	2.521	0.039	6.261	0.051	2.338	0.026	B
G79.42+2.4	0.424	0.004	4.756	0.090	0.434	0.003	8.598	0.067	0.429	0.003	6.395	0.066	C
G79.96+0.9	0.388	0.005	4.299	0.100	0.354	0.005	5.050	0.093	0.371	0.004	4.659	0.069	C
G80.35+0.7	1.529	0.007	1.785	0.010	1.553	0.015	2.022	0.024	1.541	0.008	1.900	0.013	C
G80.88+0.4	1.530	0.004	2.871	0.026	1.441	0.009	2.627	0.033	1.486	0.005	2.747	0.021	D
G80.94-0.1	7.721	0.025	1.634	0.008	7.648	0.063	1.576	0.016	7.684	0.034	1.605	0.009	B
G81.25+1.1	1.121	0.004	6.672	0.056	1.163	0.007	6.392	0.105	1.142	0.004	6.530	0.060	D
DR21	35.969	0.157	1.981	0.010	36.966	0.140	1.447	0.006	36.467	0.105	1.693	0.006	A
G82.57+0.4	1.605	0.016	6.250	0.073	1.580	0.009	3.434	0.026	1.593	0.009	4.633	0.032	C
S112	0.713	0.004	4.226	0.039	0.690	0.003	5.001	0.036	0.701	0.003	4.597	0.027	C
G85.24+0.0	1.036	0.009	2.315	0.023	1.077	0.015	2.448	0.040	1.056	0.009	2.381	0.023	C
S127A	0.739	0.005	1.552	0.013	0.730	0.009	1.833	0.026	0.734	0.005	1.687	0.014	A
WB85A	0.696	0.005	1.576	0.013	0.707	0.006	1.815	0.019	0.701	0.004	1.691	0.011	B
S128	0.989	0.008	1.515	0.015	0.963	0.004	1.571	0.008	0.976	0.005	1.542	0.008	A
S146	3.493	0.015	1.526	0.008	3.423	0.024	1.548	0.012	3.458	0.014	1.537	0.007	A

Table 3—Continued

Name	R.A.				Decl.				Average				QF
	$T_C$ (K)	$\sigma T_C$ (K)	$\Theta$ ( $l$ )	$\sigma \Theta$ ( $l$ )	$T_C$ (K)	$\sigma T_C$ (K)	$\Theta$ ( $l$ )	$\sigma \Theta$ ( $l$ )	$T_C$ (K)	$\sigma T_C$ (K)	$\Theta$ ( $l$ )	$\sigma \Theta$ ( $l$ )	
S147	0.816	0.005	1.584	0.011	0.803	0.005	1.606	0.011	0.809	0.003	1.595	0.008	A
S152	2.073	0.006	1.501	0.005	2.107	0.015	1.569	0.013	2.090	0.008	1.535	0.007	A
S156	3.494	0.011	1.498	0.006	3.544	0.016	1.474	0.008	3.519	0.010	1.486	0.005	A
NGC7538	12.121	0.078	1.978	0.019	12.129	0.120	2.236	0.029	12.125	0.072	2.103	0.017	C
S159	1.967	0.004	1.503	0.004	2.040	0.007	1.528	0.007	2.004	0.004	1.516	0.004	B
S162	1.282	0.015	2.283	0.033	1.345	0.013	1.840	0.031	1.313	0.010	2.050	0.023	B
S168	0.497	0.007	2.923	0.061	0.500	0.005	2.185	0.040	0.499	0.004	2.527	0.035	B
WB380	0.557	0.006	1.396	0.018	0.578	0.004	1.422	0.012	0.567	0.004	1.409	0.011	B
S186	0.255	0.004	1.385	0.025	0.243	0.004	1.386	0.027	0.249	0.003	1.385	0.019	B
WB399B	0.094	0.002	1.432	0.028	0.090	0.002	1.326	0.040	0.092	0.001	1.378	0.024	B
G132.16-0.7	1.004	0.007	2.889	0.022	1.068	0.005	1.474	0.008	1.036	0.004	2.064	0.010	B
W3	50.895	0.439	1.708	0.022	50.161	0.000	1.543	0.005	50.528	0.219	1.624	0.011	B
G133.790+1.4	9.927	0.097	2.376	0.028	10.127	0.051	2.288	0.017	10.027	0.055	2.332	0.016	B
G136.91+1.0	0.285	0.005	8.067	0.171	0.255	0.005	6.997	0.182	0.270	0.004	7.513	0.126	C
S201	0.869	0.016	2.091	0.044	0.774	0.007	1.771	0.017	0.822	0.008	1.924	0.022	C
S206	3.324	0.037	2.146	0.033	3.214	0.021	2.758	0.023	3.269	0.021	2.433	0.022	B
S209	2.890	0.024	2.956	0.047	3.015	0.019	2.628	0.026	2.952	0.015	2.787	0.026	B
S211	0.753	0.005	1.797	0.014	0.735	0.003	1.809	0.009	0.744	0.003	1.803	0.008	A
S212	0.654	0.007	2.985	0.040	0.639	0.005	2.929	0.029	0.647	0.005	2.957	0.025	B
S228	0.712	0.006	1.839	0.018	0.685	0.009	1.853	0.028	0.699	0.005	1.846	0.017	B
S235	0.769	0.005	4.244	0.032	0.774	0.006	3.603	0.034	0.772	0.004	3.910	0.024	B
S237	0.666	0.011	1.852	0.036	0.672	0.004	1.951	0.013	0.669	0.006	1.901	0.020	A
S257	1.072	0.010	2.401	0.027	1.109	0.008	2.516	0.021	1.090	0.006	2.458	0.017	B
S269	0.805	0.004	1.902	0.011	0.788	0.006	1.702	0.014	0.797	0.003	1.799	0.009	A
G201.6+1.6	0.277	0.003	2.233	0.055	0.441	0.004	3.795	0.069	0.359	0.003	2.911	0.044	D
OriA	110.540	1.610	2.771	0.057	111.040	0.440	3.430	0.016	110.790	0.835	3.083	0.033	B
WB870	1.233	0.009	1.420	0.012	1.188	0.007	1.436	0.009	1.211	0.006	1.428	0.008	B
MONR2	12.545	0.063	1.416	0.008	12.590	0.057	1.439	0.008	12.568	0.043	1.428	0.006	A
S288	1.212	0.010	1.780	0.021	1.556	0.008	2.034	0.018	1.384	0.006	1.903	0.014	D
WB952	1.054	0.005	1.516	0.008	1.049	0.000	1.489	0.005	1.052	0.002	1.502	0.005	B
S291	0.121	0.002	3.550	0.110	0.108	0.001	3.757	0.063	0.114	0.001	3.652	0.064	C
S297	0.355	0.006	2.268	0.047	0.352	0.004	2.698	0.033	0.354	0.004	2.474	0.030	B
S298	0.297	0.003	3.341	0.045	0.325	0.004	2.770	0.060	0.311	0.003	3.042	0.039	C
RCW6	0.398	0.004	3.768	0.052	0.437	0.004	5.610	0.056	0.418	0.003	4.597	0.039	C
RCW8	0.659	0.008	2.554	0.045	0.663	0.010	2.795	0.053	0.661	0.006	2.672	0.035	B
S305	0.649	0.011	2.807	0.058	0.641	0.009	2.975	0.053	0.645	0.007	2.890	0.039	B
S311	1.235	0.016	4.861	0.096	1.241	0.033	4.683	0.171	1.238	0.019	4.771	0.099	C

Table 4. GBT Sample: LTE Electron Temperature Radial Gradient Fits

Az Range (deg)	$a$ (K)	$b$ (K kpc <sup>-1</sup> )	r	N	$\Delta R_{\text{gal}}$ (kpc)
0 – 360	6404 ± 442	257 ± 43	0.689 ± 0.069	72	4.7 – 21.9
	6404 ± 501	257 ± 50	...	...	...
330 – 360	4448 ± 895	455 ± 87	0.77 ± 0.12	12	8.5 – 16.4
	4419 ± 1258	458 ± 120	...	...	...
0 – 30	7104 ± 425	179 ± 35	0.62 ± 0.19	33	6.0 – 17.3
	7105 ± 454	178 ± 38	...	...	...
30 – 60	4874 ± 309	389 ± 31	0.885 ± 0.082	16	4.7 – 16.4
	4876 ± 343	388 ± 35	...	...	...

Note. — Gradient fit defined by  $T_e = a + b R_{\text{gal}}$ . The second fit uses jackknife resampling.

Table 5. Green Bank Sample: LTE Electron Temperature Radial Gradient Fits

Az Range (deg)	$a$ (K)	$b$ (K kpc <sup>-1</sup> )	r	N	$\Delta R_{\text{gal}}$ (kpc)
0 – 360	5756 ± 303	299 ± 31	0.669 ± 0.052	133	0.1 – 21.9
	5756 ± 315	299 ± 33	...	...	...
330 – 360	4977 ± 718	391 ± 73	0.778 ± 0.066	24	2.0 – 16.4
	4971 ± 837	392 ± 84	...	...	...
0 – 30	6511 ± 303	228 ± 25	0.74 ± 0.104	43	4.3 – 17.3
	6511 ± 316	228 ± 26	...	...	...
30 – 60	4758 ± 499	404 ± 40	0.76 ± 0.15	28	3.7 – 16.4
	4758 ± 516	404 ± 42	...	...	...

Note. — Gradient fit defined by  $T_e = a + b R_{\text{gal}}$ . The second fit uses jackknife resampling.

Table 6. O/H Radial Gradient Fits

Az Range (deg)	GBT Sample		Green Bank Sample	
	$a$ (dex)	$b$ (dex kpc <sup>-1</sup> )	$a$ (dex)	$b$ (dex kpc <sup>-1</sup> )
0 – 360	8.866 ± 0.066	–0.0383 ± 0.0065	8.962 ± 0.045	–0.0446 ± 0.0046
	8.866 ± 0.075	–0.0383 ± 0.0074	8.962 ± 0.047	–0.0446 ± 0.0049
330 – 360	9.16 ± 0.13	–0.068 ± 0.013	9.08 ± 0.11	–0.058 ± 0.011
	9.16 ± 0.19	–0.068 ± 0.018	9.08 ± 0.13	–0.058 ± 0.013
0 – 30	8.762 ± 0.063	–0.0266 ± 0.0053	8.850 ± 0.045	–0.0339 ± 0.0037
	8.761 ± 0.068	–0.0266 ± 0.0057	8.850 ± 0.047	–0.0339 ± 0.0039
30 – 60	9.094 ± 0.046	–0.0579 ± 0.0046	9.111 ± 0.074	–0.0602 ± 0.0060
	9.093 ± 0.051	–0.0579 ± 0.0053	9.111 ± 0.077	–0.0602 ± 0.0063

Note. — Gradient fit defined by  $12 + \text{Log}(\text{O}/\text{H}) = a + b R_{\text{gal}}$ . The second fit uses jackknife resampling.

Table 7. 3C147 DCR Continuum Calibration

Frequency (MHz)	Bandwidth (MHz)	Pol.	Intensity (K)	FWHM (arcmin)	CF
8665.0000	320.0000	LL	$9.1427 \pm 0.1240$	$83.7267 \pm 1.1384$	1.018
8665.0000	320.0000	RR	$8.9200 \pm 0.1303$	$83.2861 \pm 0.6417$	1.043
8045.6050	80.0000	LL	$9.4322 \pm 0.0053$	$91.0121 \pm 0.0165$	1.053
8045.6050	80.0000	RR	$9.2940 \pm 0.0940$	$91.2244 \pm 0.1271$	1.069
8300.0000	80.0000	LL	$8.7954 \pm 0.0412$	$86.2657 \pm 1.3826$	1.099
8300.0000	80.0000	RR	$8.9534 \pm 0.0404$	$86.3678 \pm 1.0142$	1.079
8584.8232	80.0000	LL	$8.9331 \pm 0.1130$	$85.7964 \pm 0.9476$	1.050
8584.8232	80.0000	RR	$8.7353 \pm 0.1283$	$86.0558 \pm 1.1671$	1.074
8665.3000	80.0000	LL	$9.1793 \pm 0.0078$	$84.2725 \pm 0.2749$	1.014
8665.3000	80.0000	RR	$9.0220 \pm 0.0277$	$84.1787 \pm 0.9257$	1.031
8877.0000	80.0000	LL	$9.6489 \pm 0.0450$	$80.6957 \pm 1.6937$	0.944
8877.0000	80.0000	RR	$8.5722 \pm 0.0327$	$80.8070 \pm 1.2275$	1.063
9183.0000	80.0000	LL	$8.2036 \pm 0.0726$	$79.6762 \pm 1.4276$	1.078
9183.0000	80.0000	RR	$8.5481 \pm 0.1100$	$79.1310 \pm 1.1645$	1.034
9505.0000	80.0000	LL	$8.2952 \pm 0.2131$	$78.0025 \pm 1.5026$	1.034
9505.0000	80.0000	RR	$7.8862 \pm 0.1243$	$77.3615 \pm 1.7872$	1.088
9812.0000	80.0000	LL	$7.5754 \pm 0.1698$	$73.7876 \pm 0.9622$	1.101
9812.0000	80.0000	RR	$8.2367 \pm 0.1512$	$74.0209 \pm 0.6705$	1.013

Note. — Data taken on 6 January 2008 at Hour Angle =  $-1.8$  hr and elevation =  $67^\circ$ .